

SUSSEX UNIV BRIGHTON (ENGLAND) SCHOOL OF ENGINEERING--ETC F/6 11/6
SPLAT-QUENCHING OF ZIRCONIUM ALLOYS, WITH SPECIAL REFERENCE TO --ETC(U)
NOV 79 S BANERJEE N00014-78-6-0048
RD-1 NL

TR-3

100

END
DATE
FILMED
8 80
BTIC

Code
2627

SECURITY CLASSIFICATION OF THIS PAGE (When Data Entered)

①

ADA 086847

REPORT DOCUMENTATION PAGE		READ INSTRUCTIONS BEFORE COMPLETING FORM
1. REPORT NUMBER	2. GOVT ACCESSION NO.	3. RECIPIENT'S CATALOG NUMBER
Technical Report No. 3	AD-AD86 847	
4. TITLE (and Subtitle)		5. TYPE OF REPORT & PERIOD COVERED
Splat-Quenching of Zirconium Alloys, with Special Reference to Martensite and Precipitate Reactions.		Technical Report, M, 178
7. AUTHOR(s)		6. PERFORMING ORG. REPORT NUMBER
Dr Srikumar/Banerjee		1-1-78 (Apr 79)
9. PERFORMING ORGANIZATION NAME AND ADDRESS		8. CONTRACT OR GRANT NUMBER(s)
School of Engineering & Applied Sciences, Sussex University.		N-00014-78-G-0048
11. CONTROLLING OFFICE NAME AND ADDRESS		10. PROGRAM ELEMENT, PROJECT, TASK AREA & WORK UNIT NUMBERS
12. REPORT DATE		13. NUMBER OF PAGES
15th November 1979		55
14. SECURITY CLASS. (of this report)		15a. DECLASSIFICATION/DOWNGRADING SCHEDULE
Unclassified		
16. DISTRIBUTION STATEMENT (of this Report)		
Unlimited		
APPROVED FOR PUBLIC RELEASE DISTRIBUTION UNLIMITED		
17. DISTRIBUTION STATEMENT (of the abstract entered in Block 20, if different from Report)		
18. SUPPLEMENTARY NOTES		
The work described in this Report will form the subject matter of 3 papers being prepared for publication. Dr. Banerjee (a visitor from the Bhabha Atomic Research Center, Bombay), was personally supported by the Science Research Council (UK), working as a member of the QNR-supported splat-quenching group.		
19. KEY WORDS (Continue on reverse side if necessary and identify by block number)		
Zirconium, transformations, splat-quenching		
20. ABSTRACT (Continue on reverse side if necessary and identify by block number)		
A detailed TEM study is reported of the structure of splat-quenched zirconium alloys as follows: Zr-Nb, various compositions; Zr-27at%Al; Zr-14at%Ni; Zr-24at%Fe. The details of martensite and omega morphology in Zr-Nb, spinodal and precipitation reactions in Zr-Al, and the crystallisation of the amorphous phase in Zr-Ni and Zr-Fe are all fully described. In Zr-Fe, a novel morphology is described: a circular core of β surrounded by six twin-related 'petals' of α , forms a 'sunflower' pattern not hitherto reported.		

DD FORM 1 JAN 73 1473

EDITION OF 1 NOV 65 IS OBSOLETE
S/N 0102-LF-014-4601

UNCLASSIFIED
SECURITY CLASSIFICATION OF THIS PAGE (When Data Entered)

DDC FILE COPY

80 7 10 080

REPORT ON RESEARCH PERFORMED IN THE MATERIALS SCIENCE DIVISION, SUSSEX
UNIVERSITY, MAY 1978 - APRIL 1979, BY DR. S. BANERJEE, SENIOR VISITING
FELLOW

Splat-Quenching of Zirconium Alloys

1 Background and Aim

In several alloy systems a series of successive phase transformation events occur during splat-quenching and it is often possible to study such a sequence from an investigation of the final microstructure which retains some characteristic features of each of these transformation steps. Some recent investigations (1,2,3) on the structure of splat-quenched ferrous alloys have indicated that the transformation sequence does not always take the usual course, namely liquid $\rightarrow \delta \rightarrow \gamma \rightarrow \alpha$. Also there are several alternative mechanisms for each of these transformation steps, the composition of the alloy and the cooling rates at relevant temperatures being the factors responsible for the selection of the operative mechanism. The first step, i.e. solidification, may or may not involve solute segregation and the resulting morphology of the solidification product is strongly influenced by the extent of solute segregation possible during the rapid quenching treatment. Subsequent solid state transformations can occur by any of the following mechanisms:

Thermally Activated

- i) Long-range diffusional process
- ii) Massive transformations

Athermal

- iii) Martensitic transformation
- iv) Displacive transformation-like omega transformation

Transformations involving long-range diffusion are, however not encountered very often, since the quenching rate obtained in splat-quenching, even during cooling down in the solid state, is quite high. The massive and the martensitic reactions have been found to be competitive in pure iron (4) while in iron-nickel alloys the massive transformation is suppressed and the $\gamma \rightarrow \delta$ transformation occurred martensitically (5). Another interesting observation has been that the M_s temperatures in splat-quenched iron-nickel alloys are significantly lower than those reported for the same alloys quenched from the austenitic phase field.

The foregoing observations on splat-quenched alloys have stimulated further research activities in those alloy systems which during splat-quenching undergo solid-state transformations subsequent to the solidification process. Against this background, the investigation on the structure of splat-quenched zirconium alloys was taken up with a view to studying martensitic and ordering reactions. A set of zirconium-niobium alloys was selected for the investigation on martensite and the following aspects were studied:

- 1) Sequences of transformations in zirconium-niobium alloys of compositions corresponding to different stabilities of the α (hcp)

and the β (bcc) phases.

ii) The influence of splat-quenching treatment on the martensitic ($\beta \rightarrow \alpha$) and the displacive ($\beta \rightarrow \omega$) transformations in these alloys.

iii) The solidification structure of splat-quenched alloys and the influence of the pattern of microsegregation on the morphology of the martensite product.

The ordering transformation was studied in or near stoichiometric Zr_3Al alloy (Zr - 27 at%Al). The intermetallic compound, Zr_3Al , exhibits two closely related structures - the metastable DO_{19} structure when this compound is precipitated from a supersaturated α - solid solution (6), and the equilibrium Ll_2 structure when this results from a peritectoid reaction (7). The former structure, however, was encountered only in a hypostoichiometric alloy. Splat-quenching was employed on the Zr - 27 at%Al alloy with the expectation that aluminium will be retained in a disordered solid solution at a level much above the solubility limit and ordering would occur as a post-solidification process. Under equilibrium cooling from the liquid phase this alloy goes through the two-phase field, $\beta + \text{Zr}_2\text{Al}$, before entering into the Zr_3Al phase field. But it was difficult to predict in which phase this alloy would first solidify under splat-quenching conditions as aluminium is known to be a very strong α stabilizer. The experiment finally showed that the splat-quenched alloy contained ordered particles of Zr_2Al in the β matrix. The mechanism of this ordering reaction was studied.

Many of the binary phase diagrams of zirconium alloys (e.g. Zr-Ni, Zr-Fe, Zr-Cu etc.) exhibit deep eutectics and it has been possible to make amorphous alloys in wide ranges of compositions in these systems (8,9). Most of the previous investigators who studied amorphous alloys of zirconium have concentrated on compositions at or near eutectics between the intermetallic compounds of zirconium. Very little work has been carried out in zirconium-rich compositions where a eutectic point exists between the terminal solid solution (β phase) and a zirconium-rich intermetallic compound. In the present work, an attempt was made to study the formation and the crystallisation of amorphous phases in a few zirconium-rich Zr-Fe and Zr-Ni alloys, with the following aims:

i) To investigate the structure of the two-piston splat-quenched and melt-spun samples of Zr-24%Fe and Zr-24%Ni* alloys and to examine whether by a suitable selection of operating parameters it is possible to make these alloys fully or partially amorphous.

ii) To study the structure of a hypoeutectic alloy, Zr-15%Fe, which solidifies through a wide range of temperature, the gap between the liquidus and solidus temperatures being about 350°C.

iii) To follow the progress of the crystallization process in the Zr-24%Fe and the Zr-24%Ni alloys in which one expects two phases - a terminal solid solution (either α or β) and an intermetallic compound - to emerge during crystallization.

* All compositions are expressed in atom percent.

2 Experimental

Rapid quenching from the liquid state was carried out using two different techniques:

i) The two-piston splat-quenching apparatus described elsewhere (10) was used for both high-melting and low-melting alloys, as in this apparatus alloys could be melted in inert atmosphere by levitation-melting.

ii) Melt-spinning was employed only for low-melting Zr-Ni and Zr-Fe eutectics. High-melting zirconium alloys could not be melt-spun as it was not possible to find a suitable refractory nozzle which would not react with molten zirconium alloys at about 1800°C.

During levitation-melting, two different techniques were used for holding the specimens. In one set of experiments, samples were allowed to rest on a silica funnel which was used to protect the levitation coil. These samples were levitated but, during melting, intermittent contact between the silica funnel and the molten drop could not be avoided. This resulted in silicon and oxygen pick-up in these samples. In the second set of experiments, samples were suspended by zirconium wire (0.5 mm dia) inside the levitation coil which was not protected by a silica funnel. These samples, in the molten condition, did not come into contact with any crucible material and thus did not pick up impurities during melting.

Structural investigations were carried out by x-ray diffraction, optical microscopy and transmission electron microscopy. All TEM samples here prepared by electro-polishing (50-150µm thick) and melt-spun ribbons about 50µm thick). Samples obtained by the two-piston splat-quenching technique were disc-shaped. The central region of these discs (about 1.5 cm dia) had almost uniform thickness while the fringes at the periphery had gradually decreasing thickness. Some of the latter regions were electron transparent but the structure of these regions was not representative of the bulk structure so TEM investigations were confined to the electropolished samples taken from the central thick regions.

The investigations of crystallization were carried out in a differential scanning calorimeter by continuous heating experiments. In order to follow the structural changes associated with important thermal events occurring during the crystallization process, specimens were rapidly cooled (320 K/min) from different temperature levels and the structure of these specimens was studied by x-ray diffraction and TEM.

3 Results and Discussion

3.1 Sequence of Phase Transformations in Splat Quenched Zr-Nb Alloys.

From the information available on phase transformations in β -quenched Zr-Nb alloys (11), the set of Zr-Nb alloys investigated here can be divided into two groups: alloys containing up to 5.5at%Nb and those richer in Nb (10-20at%). The former group was expected to exhibit a $Liq \rightarrow \beta \rightarrow \alpha$ sequence, the $\beta \rightarrow \alpha$ transformation occurring through the martensitic mode. In the latter group, as the M_s ($\beta \rightarrow \alpha$) temperature is lower than room temperature, one would expect β -retention or $\beta \rightarrow \omega$ displacive transformation.

In splat-quenched alloys we noticed some departures from these expected sequences. In samples of unalloyed zirconium and the Zr-2.5%Nb alloy

which picked up oxygen and silicon during melting, a fine-scale cellular structure was noticed (Fig. 1). SAD and dark field microscopu revealed that these cells where of the α phase and several neighbouring cells made up a single α -grain. A distribution of the second phase along these cell boundaries was observed. This typical solidification structure of the α phase and the absence of martensitic α' suggested that the α phase formed directly from the liquid. This can happen due to one or both of the following reasons:

i) The high degree of supercooling introduced by the splat quenching treatment might be responsible for the direct $\text{Liq} \rightarrow \alpha$ transformation, skipping the intermediate β phase. Fig. 2, constructed from Kaufman's data on pure zirconium, shows that a supercooling of about 300K is necessary for making such a transformation thermodynamically possible.

ii) Oxygen contamination might have stabilized the α phase, silicon being a neutral additive with respect to the stabilization of the α and the β phases (13).

Oxygen analyses of the splat-quenched samples showed that the levels of oxygen in these are not as much as to make the $\text{liq} \rightarrow \alpha$ transformation possible under equilibrium cooling. So it was concluded that both these factors were responsible for direct α -solidification. A schematic construction in Fig. 2 illustrates how the extent of supercooling necessary for $\text{Liq} \rightarrow \alpha$ transformation is reduced by introduction of oxygen in zirconium.

The samples of zirconium and dilute Zr-Nb alloys which did not pick up any impurities during melting and splat-quenching treatment showed a normal $\text{Liq} \rightarrow \beta \rightarrow \alpha'$ (martensite) sequence. However, in some Zr-5.5Nb samples the $\beta \rightarrow \alpha'$ transformation was suppressed and the β phase underwent a $\beta \rightarrow \omega$ transformation (Fig. 3). Solid-state quenching results have shown that $\beta \rightarrow \omega$ transformation occurs in preference to $\beta \rightarrow \alpha$ only in alloys containing more than about 7Nb, the composition at which the $M_S(\omega)$ and $M_S(\alpha)$ curves intersect (Fig. 4). The present observation may indicate that the $M_S(\alpha)$ is depressed more than $M_S(\omega)$ as a faster cooling rate is employed in splat-quenching, but it is contradictory to the observations of Stewart et al (14) who have shown that the $M_S(\alpha)$ and the $M_S(\omega)$ temperatures in solid-state-quenched samples are depressed by 50°C and 100°C respectively as the cooling rate is raised from 800°C/sec to 5000°C/sec. It seems possible that the splat-quenched alloy behaves differently because of the retention of excess vacancies which stabilize ω -embryos. The proposed structural model (15) or ω -embryos which have been shown to be present in ω -forming alloys (and in Zr-Nb alloys in particular) at temperatures much above the $M_S(\omega)$ temperature consists of a vacancy around which a row of atoms is displaced along a $\langle 111 \rangle$ direction. Such embryos condense into ω particles upon cooling through the $M_S(\omega)$ temperature.

3.2 Solidification Structure in Zr-Nb Alloys Samples Containing Si and O

The samples which solidified directly into the α phase showed a fine cellular structure (Fig. 5). In order to identify the segregating species which was responsible for generating this structure, microbeam x-ray analysis of the cell interior and cell boundaries was carried out in a borrowed electron microscope operating in the STEM mode. The results clearly indicated that the cell boundaries were rich in Si which was picked up from the silica funnel during melting. SAD patterns from the cell boundary phase could be indexed in terms of an ordered tetragonal structure based on the bcc β -zirconium lattice. Close

similarity of this structure with the reported Zr_3Si and Nb_3Si structures suggested that the cell-boundary phase is $(Zr,Nb)_3Si$. α -cells were often found to contain small-angle tilt and twist boundaries, indicating that these cells were fragmented into smaller 'subgrains' (Fig. 6).

The samples which first solidified into the β -phase and subsequently transformed martensitically, exhibited a martensitic morphology superimposed on a cellular structure (Fig. 7). Unalloyed Zr and the Zr-2.5 Nb alloy showed lath morphology and the laths in these alloys were found to be continuous across cell boundaries. This was crystallographically possible as the orientations of a group of cells belonging to a grain were more or less the same. The mechanism of the propagation of martensite laths through the cell boundary has been discussed later. In the Zr-5.5Nb alloy which showed a plate martensite morphology the plates were found to be confined within the cells. This resulted in a considerable refinement of the martensite plate size (Fig. 8). SAD patterns taken from the interior of the cells showed superimposed zones of hcp reciprocal lattice sections which could be indexed in terms of different Burgers variants arising from a single β crystal (Fig. 9). DF images using strong α reflections showed the distribution of martensitic plates of a specific variant in the neighbouring cells belonging to a single β grain, but in no case were the plates seen to penetrate through cell boundaries (Fig. 10).

Samples free from Si and O contamination

Solidification structure showed cellular and sometimes dendritic appearance in the splat-quenched Zr-2.5 Nb, Zr-5.5Nb and Zr-10Nb alloys. But this was on a much coarser scale and could be resolved by optical microscopy (Fig. 11). TEM observations did not show any fine-scale segregation. In some regions of these samples very fine equiaxed grains were seen (Fig. 3). Such regions appeared to have formed by a diffusionless solidification process, presumably due to faster cooling rates.

In view of the small gap between the solidus and the liquidus curves, the occurrence of microsegregation in these splat-quenched Zr-Nb alloys was quite unexpected. If one assumes that the locus of the T_0 temperature, where $G_x^{\alpha} = G_x^{\beta}$, is midway between the liquidus and the solidus, the supercooling required to make the diffusionless solidification thermodynamically possible is not more than $10^{\circ}C$. The tendency of Nb atoms to segregate towards the liquid phase can be explained on the basis of a hypothetical $G-x$ plot (Fig. 12). The fact that a minimum in the solidus/liquidus exists at around 20%Nb is taken into account while constructing this hypothetical diagram. For an alloy of composition 5.5%Nb which has a T_0 temperature higher than T , the chemical potential of Nb atoms in liquid-phase μ_{Nb}^{Liq} is much smaller than μ_{Nb}^{β} , hence Nb atoms show a tendency to remain in the liquid phase as the solidification front gradually progresses. The thermodynamics of the overall reaction is also favourable as the mixture of Nb-rich liquid phase and solute-depleted β phase has a lower free energy than that of the parent liquid. According to this argument, in an alloy containing 20%Nb, such segregation tendency should be absent and solidification was expected to be diffusionless as was indeed observed (Fig. 13).

3.3 Martensite Morphology and Substructure in Splat-Quenched Zr-Nb Alloys

Samples containing Si and O

In lath martensite structure of the dilute alloys martensite laths were seen to be continuous across the cell boundaries. But in Zr-5.5Nb which showed a plate morphology, plates were confined within the cells. The former observation indicates that immediately before the formation of lath martensite, there existed a continuity of lattice from one cell to its neighbour. It seems possible that at that stage a β -grain consisted of several solute depleted cells separated by solute rich boundaries but the average lattice within a grain was continuous. Since the silicide structure can be viewed as a superlattice structure based on the β -zirconium lattice, we imagine that the long range order necessary to generate the silicide superlattice was not established before the formation of lath martensite. Hence it was possible for the transformation shear to propagate through these silicon rich cell boundaries. The ordering reaction occurred subsequently to produce a distribution of silicide phase along these boundaries. In the Zr-5.5Nb alloy where martensitic transformation occurred at a much lower temperature resulting in the plate morphology, the ordering of the cell boundary regions to form the silicide phase appeared to have occurred prior to the martensitic transformation. Consequently β grains were partitioned by silicide cell walls which prevented the growth of martensite plates across these boundaries.

Samples free from Si and O contamination

Two distinct martensite morphologies - plate and lath-were observed in this set of splat-quenched Zr-Nb alloys. The lath morphology which was exhibited by unalloyed zirconium and the Zr-2.5Nb alloy is characterized by parallel stacking of martensite laths. There is, however, a significant difference in the interlath orientation relations observed in lath martensite obtained in β -quenched dilute Zr-Nb alloys (16) and those observed in splat-quenched Zr-2.5Nb alloy. In β -quenched samples, adjacent laths always showed a small-angle boundary between them which means all the laths in a packet belonged to a single variant of orientation relation with the parent β crystal. In the splat-quenched Zr-2.5Nb alloy, two distinct types of lath boundaries were observed: small-angle boundaries and twin boundaries. The former was seen to contain an array of dislocations (Fig. 14). Unambiguous determination of the Burgers vector of these dislocations was not possible but the fact that these dislocations could be imaged under (0002) reflection indicated their non-basal character. Such dislocations with non-basal Burger vector are not commonly found in deformed zirconium alloys and it appears that these dislocations were associated with the inhomogeneous shear process. Otte's calculations (16) show that slip shear along $\langle 11\bar{2}3 \rangle$ direction is the most likely inhomogeneous shear for the $\beta \rightarrow \alpha$ martensitic transformation. The presence of dislocations with non basal Burgers vector at the lath boundaries is consistent with Otte's prediction. Twin relation between the adjacent laths was frequently encountered. Fig. 15 shows the SAD pattern taken from two neighbouring laths which are related by $\{10\bar{1}1\}$ twin relation. It was seen that some packets of laths contained a stack of twin related laths, every alternate lath having the same orientation. This has been demonstrated by the dark field micrograph (Fig. 15(c)) taken with a twin reflection.

As the $\beta \rightarrow \alpha'$ martensitic transformation and the $\beta \rightarrow \omega$ transformation were found to be competitive in the Zr-5.5Nb alloy, martensite structure was observed only in some areas of these samples. Martensite in this alloy exhibited a typical plate morphology (Fig. 16). Such a transition in morphology from the lath to the plate type was noticed in the β -quenched Zr-Nb alloys at about 1% Nb (17). The present observations show that this transition is shifted to a higher level of niobium content (2.5-5%) in splat-quenched alloys. A similar observation was made in Fe-Ni alloys but we are not in a position to rationalize these observations as yet.

The lath and the plate martensites were seen to be associated with a dislocated and a twinned substructure respectively. Twinning was always on $\{10\bar{1}1\}$ planes (Fig. 17), suggesting that the transformation crystallography is of the Bowles-Mackenzie class A type. However, the substructure of this plate martensite is not as regular as that envisaged in the theory. The spacing, thickness and the ratio between the thicknesses of the two orientations of twins were not uniform. Sometimes within a single martensite plate different substructures were observed. The plate shown in Fig. 18 contains two $\{10\bar{1}1\}$ twin variants in one part while in the remaining plate only a single variant is operative. One generalization could be made from the observations on a large number of twinned martensite plates, viz., that within the thin lamellae of twins a second shear was operative. The traces corresponding to the planes on which this occurred are revealed as fine striations and can be indexed as $\{10\bar{1}1\}$ traces. This observation confirms the existence of multiple lattice-invariant shear which was reported in β -quenched Zr-Nb (17(a)) and Zr-Ti (17(b)) alloys. Another interesting crystallographic observation is shown in Fig. 19, in which two adjacent martensite plates are seen to contain a set of twins which are common to both the plates. This is possible because the three orientations α_1 , α_2 and α_3 which are mutually twin-related can have equivalent relation with a single β orientation. Another manifestation of this orientation relation has been found in the formation of composite crystals having a 'Sunflower' morphology formed during the crystallization of amorphous Zr-Fe alloy. This is discussed in detail in a later section. It can be seen in Fig. 19 that the internal twins are propagating through the boundary between the martensite plates without changing direction. This is due to the fact that the $\{10\bar{1}1\}$ twin planes in α_1 and α_2 plates are nearly parallel. Such a twin intersection is permitted by the continuity conditions proposed by Cahn (18). The area (marked x) adjacent to these plates shows a predominately ω -region as demonstrated by the SAD pattern (Fig. 19(a)). This exemplifies how the two processes, $\beta \rightarrow \omega$ and $\beta \rightarrow \alpha$ transformations, occurred side by side in this sample. In another sample of the same alloy produced under the same condition of splat-quenching, $\beta \rightarrow \omega$ transformation was found to be predominant. Variation in quenching rates from one run to another appear to be responsible for such difference in the transformation behaviour.

3.4 $\beta \rightarrow \omega$ Transformation in Zr-Nb Alloys

The athermal $\beta \rightarrow \omega$ transformation was found to occur in the splat-quenched Zr-5.5Nb, Zr-10Nb and Zr-20Nb alloys. It is now well-established (19,20) that with increasing addition of β -stabilizing elements (as the $M_s(\omega)$ temperature is lowered) the size of the as-quenched ω -particles decreases and the sharp ω -reflections become more and more diffuse. Finally, when the $M_s(\omega)$ is reduced down to room temperature or even below, the diffraction patterns from the

β -quenched samples show only a diffuse intensity distribution characteristic of linear displacement defects present in the β lattice. This general trend was also observed in the splat-quenched alloys. In the present case the $\beta \rightarrow \omega$ reaction was made possible in a more dilute alloy corresponding to a higher $M_s(\omega)$ temperature and consequently large well defined ω -particles were observed (Fig. 20). This can be seen from a comparison of the morphology of these particles with that of the particles formed in β -quenched Zr-8Nb alloy (the most dilute alloy in which ω formation was observed by Dawson and Sass (21)). The reported alignment of ω -particles along $\langle 111 \rangle_\beta$ direction was not observed. The corresponding diffraction pattern shows sharp ω -reflections with only a limited streaking. All these observations suggest that the ω -phase in the splat quenched Zr-5.5Nb alloy formed at a relatively high temperature and the larger gap between the $M_s(\omega)$ and the room temperature was responsible for coarsening of these particles. Isolated α -martensite plates were noticed in the matrix of β/ω (Fig. 21). This again shows the competition between the two athermal transformation processes. It is apparent that these martensite plates did not get a chance to grow or to induce further α -nucleation by autocatalysis as the $\beta \rightarrow \omega$ transformation occurred in the matrix almost simultaneously. A distribution of much finer α -particles still (about 100 - 200 Å in size) was noticed in some regions. The presence of these fine α -particles could be detected in the SAD pattern corresponding to $\langle 100 \rangle_\beta$ zones in which allowed ω -reflections superimpose on β -reflections. In this zone extra reflections at $\frac{1}{2}$ 110_β and 100_β positions could be indexed as α -reflections (Fig. 22).

With the increase in Nb content ω -particle size decreased but it was possible to resolve the morphology of the ω -particles in Zr-10Nb (Fig. 23). In this alloy also extra reflections due to fine α -particles were noticed (Fig. 24). In view of the fact that ω -particles act as precursors for α -nucleation during ageing, it seems possible that some ω -particles transformed to the α phase during cooling down from the $M_s(\omega)$ temperature. It is, however, not clear how the $\omega \rightarrow \alpha$ transformation could occur in such a short time.

In the splat-quenched Zr-20Nb alloy the β phase was retained. The SAD pattern shows diffuse intensity distribution as shown in Fig. 25. This diffused intensity was found to be along $\{111\}$ reciprocal lattice planes confirming the presence of instability of $\{111\}$ planes near the $M_s(\omega)$ temperature. The maxima of these intensity distributions are close to the ω -positions but a systematic displacement of the diffuse intensity near $\{1010\}_\omega$ reflections can be noticed. Such displacements have been reported in β -quenched alloys and have been attributed to a configuration in which (111) planes are not fully collapsed to the middle (see Fig. 33).

The splat-quenched Zr-20Nb alloy showed another phase which exhibited a Widmanstätten morphology (Fig. 26). A precipitate phase (β'') of similar morphology was observed earlier (22) and has been assigned tetragonal structure with $a = 3.52$ Å and $c/a = 1.13$. TEM observations made in this work showed that the interfaces between the Widmanstätten plates and the matrix were not well defined. This appears to be due to the existence of the one-to-one lattice correspondence, i.e. $\langle 100 \rangle_\beta // \langle 100 \rangle_{\beta''}$, and the small difference in the lattice spacings of the two phases. Dark-field images with a ω -reflection shows a higher density of ω -particles within the β'' plates suggesting that this phase has a smaller concentration of Nb. This is consistent with the fact that the β'' phase has a larger unit cell volume than

the matrix β phase. The tendency to phase separation (23), as reflected in the miscibility gap in the β phase field, appears to be responsible for the formation of β'' phase.

3.5 Formation of an "Ordered Omega Phase" in the Splat Quenched Zr-27at%Al Alloy

The splat-quenched structure showed grains with undulating boundaries and a distribution of second-phase particles within these grains (Fig. 27). X-ray and electron diffraction revealed that the matrix grains were of the β phase. The morphology of these fine second-phase precipitates suggested that the precipitation occurred in the solid state. This implied that the eutectic reaction was suppressed under splat quenching condition and that the liquid alloy solidified into a supersaturated β phase from which the second phase particles precipitated out. The origin of the undulating shape of grain boundaries was not clear. Such boundaries might have developed either during the solidification process as a result of morphological instability of the liquid-solid interface or extensive grain boundary migration might have occurred after the β grains had solidified. In the majority of these grains, no sign of microsegregation was present but in some grains a cellular structure was noticed. A uniform distribution of precipitates was observed in the former while in the latter the cell boundaries were decorated by more densely populated precipitates (Fig. 28).

SAD patterns taken from different grains could be indexed in terms of different sections of the bcc reciprocal lattice with 'extra' reflections appearing at $\frac{1}{3}$ bcc positions (Fig. 29). The apparent symmetry of such reciprocal lattice sections suggests that the precipitate phase has a bcc structure with lattice spacing three times that of the matrix. One should, however, consider the fact that within a matrix grain, precipitate variants are related to one another by the symmetry of the matrix and hence the symmetry of the superimposed reciprocal-lattice sections of the matrix and the several variants of the precipitate crystals will always be that of the matrix if all variants are equally probable. Dark-field microscopy from different 'extra' spots enabled us to separate each group of reflections belonging to each variant of precipitates. This analysis revealed that the second phase particles have a structure very similar to the omega phase, the four variants of the hexagonal precipitate phase maintaining the following orientation relation with the matrix: $(0001)_{\text{ppt}} \parallel 111 \text{ bcc} ; \langle 11\bar{2}0 \rangle_{\text{ppt}} \parallel \langle 1\bar{1}0 \rangle_{\text{bcc}}$.

The difference between the structure of these precipitates and that of the omega phase was revealed from the SAD patterns corresponding to $[111]_{\beta}$ and $[100]_{\beta}$ zones in which allowed β -reflections coincide with the ω -reflections. Fig. 30 shows the presence of extra reflections observed in the present case which can not be accounted as ω -reflections. A comparison of the bcc, the ω and the Zr_2Al structures (24) (as illustrated in Fig. 31), all oriented according to the observed orientation relation, shows that the Zr_2Al structure can be generated by introducing an order in the ω -structure. This ordering makes the c -axis of the ordered phase twice as long as that of ω and the ω -reflections associated with zero structure factor ($l = 2m$ and $h-k = 3n \pm 1$) appear as superlattice reflections. Since these 'extra' reflections observed in the present case could be indexed in terms of the Zr_2Al superlattice, we came to the conclusion that these precipitates

are Zr_2Al or 'ordered omega' particles. It is, however, likely that during rapid quenching process these precipitates might not have attained the exact stoichiometry and the perfect order. Another interesting observation was that the Zr_2Al precipitates were aligned along the different variants of the elastically soft $[100]_\beta$ directions, giving a modulated appearance of the microstructure when viewed along one of the cube directions. Fig. 32 exemplifies such a microstructure, the corresponding diffraction pattern showing the presence of side bands around the fundamental bcc reflections. While dark-field images using the 200_β reflections clearly revealed the striations, the superlattice dark-field images showed the distribution of precipitate particles along these striations. The wavelength of these modulations measured from the striated microstructures (150-200 Å) agreed well with that calculated from the side-band spacings. All these observations suggested that prior to the formation of the Zr_2Al precipitates this alloy decomposed spinodally to produce alternate regions depleted and rich in solute and precipitation occurred in the solute rich regions. The extreme rapidity of the spinodal decomposition in this alloy could be attributed to the anomalous diffusion of aluminium in β -zirconium.

Considering the similarity of the structure of the β , the ω and the Zr_2Al phases and the observed similarity in the lattice correspondence between β and ω on one hand and β and Zr_2Al on the other, we propose a possible mechanism of the formation of the Zr_2Al phase in the aluminium-rich regions. The athermal $\beta \rightarrow \omega$ transformation is known to be accomplished by collapsing a pair of $(111)_\beta$ planes to the intermediate position, leaving the next plane unaltered, collapsing the next pair and so on (25). This mechanism as schematically illustrated in Fig. 33 produces a structure of hexagonal symmetry which is described as the 'ideal ω -structure'. In other words, the transformation can be accomplished by submitting the β -lattice to a $\frac{2}{3}$ 111 longitudinal displacement wave of proper amplitude and phase (Fig. 33 (d)). The formation of the Zr_2Al phase can be visualized as a hybrid of displacive ω transformation and a replacive ordering reaction. The latter process can be described in terms of a short wave length concentration wave as illustrated in Fig. 34. There are two alternatives for this concentration wave description, one corresponding to a situation where such a composition fluctuation develops prior to the introduction of displacement wave and the other consisting of ω -transformation followed by setting up of the concentration wave. The former description, designated B, appears to be applicable in the present case because of the following reasons:

The fact that the $\beta \rightarrow \alpha$ transformation is suppressed in this α -stabilized alloy suggests that the formation of the Zr_2Al phase occurred at a temperature above the β/α transition temperature (around 1000°C). This is also indicated from the size of the Zr_2Al particles which are found to be much larger than athermal ω particles (20-50 Å) normally encountered in several β -quenched zirconium and titanium alloys. Though the $M_s(\omega)$ temperature for this alloy is not known, it is expected to be much lower than 1000°C, as $M_s(\omega)$ in ω -forming systems has always been reputed to be less than 600°C. This would imply transformation in the present case has occurred at a temperature where the β phase is either stable or metastable with respect to the ω -fluctuation. By setting up a short wavelength concentration wave of the type B it may be possible to make the bcc lattice more amenable for the collapse of (111) planes (as indicated in Fig. 33), because the chemical force to establish the right co-ordination for aluminium atoms in Zr_2Al and the elastic accommodation of smaller size aluminium atoms on the collapsed pair of planes will both be favoured.

In summary, we suppose the following sequence of events to have occurred during the evolution of the Zr_2Al phase in this splat-quenched alloy:

- i) The liquid alloy solidified as supersaturated β phase.
- ii) This β phase spinodally decomposed to produce alternate layers rich and depleted in aluminium.
- iii) Within the solute-rich regions, a short wavelength concentration fluctuation (as described in scheme B) develops.
- iv) $\{111\}$ lattice planes collapse in the right sequence to produce the ordered omega structure of the Zr_2Al phase.

According to this scheme, the overall reaction involves spinodal clustering, spinodal ordering and displacement ordering in succession.

3.6 Structure of Two-Piston Splat-Quenched Eutectic Alloys of Zirconium

Two-piston splat-quenching was carried out on two eutectic alloys, Zr-24%Ni and Zr-24%Fe, and one hypoeutectic alloy, Zr-15%Fe. Only the Zr-24%Ni alloy could be made partially amorphous by this technique. The iron-bearing alloys were crystalline and structural investigations on these have not been completed yet. In this section results on the Zr-24%Ni alloy are presented and discussed.

The partly amorphous Zr-24%Ni alloy showed dendrites in an amorphous matrix (Fig. 35). The morphology of these very small dendrites with very small gaps between dendrite arms which in the final structure are filled up with the amorphous phase suggests that these dendrites formed from the liquid phase and subsequently the remaining liquid was vitrified. There is a clear distinction between the morphology of these dendrites and those of crystals formed from the amorphous phase either during cooling down from the liquid/glass transition temperature or during subsequent ageing treatment.

From the internal structure of these dendrites it is possible to group them in two categories, one showing a martensite structure and the other having a distribution of fine precipitates morphologically similar to ω -precipitates (Fig. 36). This implies that β -dendrites formed from the liquid phase and that either the $\beta \rightarrow \alpha'$ or the $\beta \rightarrow \omega$ transformation occurred in these, depending upon the extent of solute rejection from these dendrites. The fact that the solidifying phase was β suggests that the supercooling imposed by the splat-quenching treatment was not higher than about 150°C, because at a higher supercooling, formation of the α -phase would be thermodynamically more favourable. At such moderate supercooling the composition range of the β phase which can form from the liquid phase of eutectic composition is not large (Fig. 37) and formation of a highly supersaturated dendrite is thermodynamically impossible.

By applying the material balance equation at the solid/liquid interface (26)

$$V = D_L \nabla C / C_L - C_S$$

where V is the velocity of the solid/liquid interface which is

about 10^{-2} to 10^{-1} m sec $^{-1}$ in a splat-quenching process (27,28). DL, the diffusion co-efficient of solute in the liquid phase ($\sim 10^{-9}$ m 2 sec $^{-1}$), ∇C is the composition gradient in the liquid adjacent to the solid, and $C_L - C_S$, the solute to be removed per unit volume converted from liquid to solid, an order-of-magnitude estimation of solute gradients at the interface can be made. Substituting appropriate values in this equation we obtain ∇C to be about 5% per micron. Such a steep composition gradient lowers the melting point of the liquid to a large extent in the immediate vicinity of the dendrite and thus prevents freezing of the narrow gap between the dendrite arms.

According to the criterion of constitutional supercooling (29), cellular or dendritic growth occurs when $G < MC_0(1/k-1) V/D$, where G is the actual temperature gradient, in the slope of the liquidus line, C_0 , the average composition of the alloy and k the distribution coefficient. An upperbound estimate of G

$$\left(= \frac{T_M - T_R}{d} = 15 \times 10^6 \text{ K m}^{-1}, \quad T_M \text{ and } T_R \text{ being the melting}$$

temperature and the room temperature respectively and d the semi-thickness of the splat, $\sim 0.25 \mu\text{m}$) is found to be orders of magnitude smaller than the right-hand side (10^{10} to 10^{11} K m $^{-1}$). This explains why morphological instability develops in this alloy at such an early stage of solidification.

3.7 Crystallization of the amorphous phase in the Zr-24^a/oFe and the Zr-24^a/oNi alloys

Zr-24^a/oNi

X-ray diffraction of melt-spun ribbons of this alloy showed diffuse intensity maxima characteristic of an amorphous phase with superimposed weak and diffused peaks (Fig. 38(a)). TEM examination revealed the presence of a small number of nearly spherical crystalline particles embedded in the amorphous matrix, the volume fraction corresponding to the crystalline phase being about 5%. SAD and dark field microscopy showed that each particle contained a single crystal core of the α phase and a thin boundary layer (Fig. 38(c)). The structure of this boundary layer could not be identified unambiguously from the diffraction patterns obtained but the d spacings associated with the extra spots in the diffraction pattern matched reasonably well with those of important Zr_2Ni reflections. The absence of martensitic structure within these particles suggested that these particles had formed either directly from the liquid phase or from the amorphous matrix as a result of "autotempering". The morphology of these particles were quite distinct from those encountered in two-piston splat-quenched samples in which dendrites were frozen in at a very early stage of their growth in the amorphous matrix.

The progress of crystallization was studied in this partly amorphous alloy by differential scanning calorimetry. Continuous heating experiments at constant heating rates showed two distinct exothermic peaks as illustrated in Fig. 39. In order to find out the phase reactions associated with these two peaks samples were cooled after attaining different temperature levels during the DSC run at the fastest available cooling rate (320 K/min). X-ray diffraction and TEM were carried out on these samples which went through the crystallization process to different extents. Fig 4.0 shows representative microstructures and diffraction patterns taken from samples fast-

cooled after tracing the first and second peaks during the DSC run. After the completion of the event I the sample showed a distribution of α -phase speckles in a matrix which still remains amorphous (as demonstrated by the halo in the diffraction pattern). A somewhat larger α -grain was observed in the sample after completion of the event II. In the latter case, the intervening space between the substructure free α grains showed a fine scale lamellar structure (Fig. 41). Most of the rings obtained in the SAD pattern could be indexed in terms of the α and the Zr_2Ni reflections. These observations implied that the event I was associated with the formation of the α crystals in the amorphous matrix while during the event II the remaining amorphous regions transformed into either Zr_2Ni or a mixture of α and Zr_2Ni . The other possibility is consistent with the observation of lamellar structure in the gap between α grains. It was, however, not possible to conclusively prove that these regions contained lamellae of the α and the Zr_2Ni phases. Such lamellar appearance might have resulted from the contrast between different domains of Zr_2Ni crystal (like perpendicular twin boundaries in tetragonal crystals).

DSC results showed that the peak positions which corresponded to the maximum rate of the crystallization process were dependant on the heating rate employed and that the separation between the peaks I and II decreased as the heating rate was reduced (Table 1). Finally, at the heating rate of only $2\frac{1}{2}$ K/min these two peaks almost merged. Applying Kissinger's method (30), the activation energies associated with these two events were evaluated and the results are presented in Fig 42. The assumption implicit in this analysis is that the fraction transformed at the peak position is independent of the heating rate. The value of the activation energy for the event I (310 KJ/mole) is comparable to those determined for crystallization of a large number of alloy glasses and that for the event II is found to be significantly smaller (164 KJ/mole). We propose the following rationalization on the basis of the results of structural investigations

During the event I, α particles nucleated and grew and this process required rejection of nickel atoms from the growing particles of the α phase which has a very low solubility of nickel. Under such a circumstance, one would expect long-range diffusion of nickel atoms away from growing α -particles to be the rate-controlling step. In the absence of any data on diffusion or viscous flow in amorphous zirconium-base alloys, no direct comparison can be made, but a good agreement between the activation energy values for the α formation in the present case and in a similar titanium-base alloy (31) ($\text{Ti}_{50}\text{Be}_{40}\text{Zr}_{10}$) lent support to the proposal that long-range diffusion of solute in the amorphous matrix is the rate-controlling step. As the event I approaches completion the remaining amorphous phase becomes progressively rich in nickel and either of the following processes occur as the event II:

- i) An eutectoid-like reaction in which $\alpha + \text{Zr}_2\text{Ni}$ form.
- ii) The amorphous phase transforms into the Zr_2Ni phase, different domains in a given region exhibiting a lamellar appearance.

The process i) is expected to involve short-range diffusion at the transformation interface and the process ii) requires short-range atomic rearrangement within the nickel-rich regions. Such processes normally involve a lower activation energy, as was indeed observed.

Apart from these processes which occurred within the amorphous matrix,

heterogeneous nucleation of α particles was observed at the boundary of the pre-existing α crystals. These heterogeneously nucleated particles were much larger than those homogeneously nucleated in the matrix (Fig. 43). This implied that the former nucleated earlier, presumably during the incubation period of the homogeneous nucleation and grew till the advancing interface of the growing α grains encountered homogeneously nucleated particles. The volume fraction of the heterogeneously nucleated crystals was so small that no thermal effect could be detected in the DSC experiments

Zr-24^a/oFe

Melt-spun samples of this alloy showed diffuse intensity maxima in the x-ray and electron diffraction patterns (Fig. 44). No crystalline particle was seen in the TEM micrographs, indicating that this alloy was fully amorphous. TEM observations revealed periodic modulations as shown in Fig. 45, the average wavelength of the modulations being about 200Å. The repetitive spacing and the connectivity of the two conjugate regions are suggestive of a spinodal decomposition in this alloy glass. A computer-simulation image of a spinodally decomposed structure (32) in an isotropic system shows a remarkable similarity with that observed in this alloy. In view of these observations and the fact that phase separation is quite common in glass forming systems (CaO₂-SiO₂, Na₂O-SiO₂, Li₂O-SiO₂ etc) we tentatively propose that this alloy underwent a spinodal decomposition. In the present case however, the "microstructural sequence" technique could not be employed to show the gradual amplification of the contrast with progressive ageing because crystallization occurred during the ageing treatment.

During continuous heating of this alloy glass, crystallization occurred in a single stage as indicated by the appearance of a single exotherm peak in the DSC plot (Fig. 46). Samples corresponding to different levels of fraction transformed were taken for x-ray diffraction and TEM studies. These investigations showed that the α phase and a zirconium rich compound phase started appearing simultaneously from the beginning of the crystallization process (Fig. 47). Crystal structures of zirconium-rich Zr-Fe compounds have not been reported as yet, only the d spacings corresponding to the Zr₄Fe and the Zr₂Fe compounds are available (33). Existence of another compound, Zr₃Fe (34), has also been reported from microprobe data obtained from a Zr-Fe diffusion couple, but no structural data are available. From the weak and diffuse peaks other than those due to the α phase it is difficult to say which of the intermetallic compounds appeared as a result of crystallization. This is more so because the reported d spacings corresponding to the intense reflections of the Zr₄Fe and the Zr₂Fe compounds are overlapping. However, the observed d spacings could be matched with the overlapping intense reflections.

The kinetics of crystallization was studied by continuous heating in a DSC at different heating rates and the result is presented in Table I and in form of an Arrhenius plot in Fig. 43. The activation energy of the process was found to be 316 KJ/mole, in close agreement with that obtained for peak I of the Zr-24^a/oNi alloy.

Microstructural observations revealed that apart from the uniformly distributed small crystals in the matrix, some large crystals almost invariably grouped in a very regular morphology (Fig. 48) were present in samples crystallized to different levels of fraction transformed.

The volume fraction occupied by these randomly distributed crystals was almost the same in all samples studied.

This suggests that these crystals formed in the initial stage before homogeneously nucleated crystals started appearing.

These composite crystals appeared like 'Sunflowers' with six petals. The central circular region ("Stamen and Pistils", if we choose these botanical terms) was not observed in all cases but the 'petals' were always found to converge to the centre. Each 'petal' exhibits a characteristic shape with faceted boundary separating the crystal and the partly crystallized matrix and two straight boundaries between one petal and its two neighbours. The overall symmetry of these 'Sunflowers' was best seen when the foil is so oriented that the corresponding diffraction pattern shows the Kikuchi star of $\langle 111 \rangle$ cubic zone (Fig. 48 (d)). Dark-field microscopy from several such flowers indicated that the orientations of opposite petals were the same, implying that such a group of crystals contains three distinct orientations of 'petals'. In some large composite crystals it was possible to obtain diffraction pattern from each individual 'petal' and from the central circular region (Fig. 49). The 'petal' were always found to be hcp phase in which a long range order is present. The lattice parameters derived from the fundamental hcp reflections were found to be close to those of α -zirconium. The central region showed a bcc structure (close to the β -zirconium phase) with diffused intensity at ω positions. Dark-field imaging with these diffused reflections showed presence of small particles (presumably ω) within the central region. Single-surface trace analysis showed that the interfaces separating adjacent petals matched with $\{10\bar{1}1\}_\alpha$ traces and the faceted boundaries of the petals corresponded with (0001) and $\{10\bar{1}1\}$ planes. Stereographic analysis showed that the adjacent petals are related by a $\{10\bar{1}1\}$ twin relation while the orientation of the β -core is approximately related with the three α -petals by three variants of Burgers relation. Accurate determination of the orientation of different crystals under the same condition of tilt of the specimen was not possible and we believe this was responsible for the observed deviation from the Burgers relation. On the basis of these observations, a crystallographic description of these 'Sunflowers' is given in a schematic diagram (Fig. 50). The formation of such symmetrical composite crystals is consistent with a Burgers orientation relation between the bcc and the hcp structures, the different orientation variants being mutually related by twin relations. In this configuration the central β region can retain crystallographically equivalent orientation relations with all the six petals, each of which maintains a $\{10\bar{1}1\}$ twin relation with its two neighbours. Since all the interfaces (α/α and α/β) within such a composite crystal are low-energy surfaces, the overall surface energy is expected to be low and this explains why these 'Sunflowers' were so frequently observed.

We can speculate about the sequence in which these composite crystals have formed. The first step involved formation of a β crystal, which occurred either during solidification or from the amorphous phase during crystallization. The α -petals nucleated on this β crystal and the aforesaid orientation relations dictated the morphology. We do not have any information on the composition of these α -petals. The equilibrium α phase is known to have very little solubility of Fe but the presence of some extra spots (presumably superlattice spots) in the SAD patterns from the α -petals suggests that they contain a higher level of Fe. The structure of the superlattice present in these has not been worked out as yet.

CONCLUSIONS

The following conclusions were reached on the basis of the observations made in the year's work;

1. On splat-quenching, dilute Zr-Nb alloys (Nb content less than about 5%) undergo a liquid $\rightarrow \beta + \alpha'$ sequence of transformation and more concentrated alloys go through a liquid $\rightarrow \beta + \omega$ sequence. This trend is similar to what is observed in β -quenched samples but the composition level where the changeover occurs from the $\beta + \alpha$ martensitic transformation to the $\beta + \omega$ transformation is found to shift to a lower Nb content in splat-quenched alloys. Presence of excess vacancies in splat-quenched alloys is thought to be responsible for favouring the $\beta + \omega$ transformation in those alloys in which martensitic and omega transformation are competitive.
2. The solidification of the α phase directly from the liquid phase is possible by splat-quenching only in alloys in which α phase-stability is increased by oxygen contamination. In these alloys the required supercooling for liquid $\rightarrow \alpha$ transformation was lowered by oxygen. (All alloys were levitation-melted, some free-floating and some with a silica guide, causing Si and O pickup).
3. In Si- and O- contaminated samples of Zr and Zr-Nb alloys (2.5 and 5at%Nb), martensite structure is observed against a background of a cellular solidification structure. Martensite laths (in Zr and Zr-2.5Nb) which formed at relatively high temperatures are continuous across the cell boundaries, whereas the martensite plates (in Zr-5.5Nb) remain confined within the cell. This is because the laths form prior to the formation of the silicide phase at the cell boundaries but the plates form after the β -grains are partitioned by silicide walls at the cell boundaries.
4. As in the case of β -quenched alloys, the (lath-to-lath) transition in morphology and the (slipped-to-twinning) transition in sub-structures of Zr-Nb martensites occur as the Nb content is increased beyond a certain level. But the transition is shifted to a higher level of Nb content (between 2.5 to 5% Nb), compared with β -quenched alloys.
5. The structure of the Zr-27at%Al alloy show a dispersion of Zr_2Al particles in the β -matrix. On the basis of the present observations the formation of the Zr_2Al phase during rapid quenching appears to involve the following steps:
 - a) Diffusionless solidification to the β phase (with only a few β grains exhibiting cellular structure).
 - b) Spinodal clustering within the β phase to produce layers (along elastically soft $\{100\}$ planes), alternately rich and depleted in Al.
 - c) Introduction of a short wavelength concentration fluctuation (spinodal ordering) within the Al rich regions.
 - d) Collapsing of $\{111\}$ planes in a manner similar to that occurring during ω -transformation.
6. Two-piston splat-quenched Zr-24at%Ni alloy shows a partially amorphous structure in which small dendrites are present in an amorphous matrix. Application of the constitutional supercooling

criterion justifies the development of dendrite morphology in this case.

7. It is possible to make the Zr-24at%Ni and the Zr-24at%Fe alloys amorphous by employing the melt-spinning technique. In the former alloy crystallization occurs in two steps: the first and the second crystallization events are the formation of the α and the Zr_2Ni ($+\alpha$) phases respectively. The activation energies associated with these steps are 310 KJ/mole and 164 KJ/mole respectively.

The amorphous phase in the Zr-24at%Fe alloy crystallizes in a single step in which the α phase and an intermetallic compound (Zr_4Fe or Zr_2Fe) form simultaneously, the activation energy of the process being 316 KJ/mole. In addition to the homogeneously nucleated crystals, some composite crystals with very regular geometrical morphology form heterogeneously during crystallization. These composite crystals (with what we have termed a 'Sunflower' morphology) are made up of a β -crystal core and six α -petals which have different variants of twin-related on $\{10\bar{1}1\}$ planes.

ACKNOWLEDGEMENTS

It is a pleasure to acknowledge many stimulating discussions with Professor R.W. Cahn and the continuous encouragement received from him. The author would like to thank Dr. B Cantor, Dr. M G Scott, Mr. G Gregan and Mr. F Duflos for many helpful discussions. The sponsorship of the Science Research Council is gratefully acknowledged. The author is thankful to the authorities of the Bhabha Atomic Research Centre for granting him a leave of absence.

REFERENCES

1. J.J. Rayment and B. Cantor, *Met. Sci. Jnl.*, 12 (1978) 156.
2. R.W.K. Honeycombe, in "Rapidly Quenched Metals III", ed. B. Cantor (Metals Society, London 1978), vol 1 p.73.
3. J.J. Rayment and B. Cantor, in "Rapidly Quenched Metals III", ed. B. Cantor (Metals Society, London 1978), vol 1 p.198.
4. F. Duflos and B. Cantor, in "Rapidly Quenched Metals III", ed. B. Cantor (Metals Society, London 1978) vol 1 p.110.
5. Y. Inokuti and B. Cantor, *Scripta Met.*, 10 (1976) 655.
6. P. Mukhopadhyay and S. Banerjee, Phase Transformations, The Inst. of Metallurgists Spring Residential Conference at York, Series 3, No.11, vol 2, 1979, p II-41.
7. E.M. Schulson, *Acta Met.*, 24, 615 (1976).
8. R. Ray, B.C. Giessen and N.J. Grant, *Scripta Met.*, 2, 357 (1968).
9. One Sussex Conf. paper from Poland, dealing with Zr-Ni, Zr-Fe crystallization.
10. R.W. Cahn, K.D. Krishnand, M. Laridjani, M. Greenholz and R. Hill, *Mat. Sci. & Eng.*, 23, 83 (1976).
11. D.L. Douglass, The Metallurgy of Zirconium, Atomic Energy Review, Supplement IAEA Viena (1971).
12. L. Kaufman and H. Bernstein in Computer Calculation of Phase Diagrams, J.L. Margrave ed., Academic Press, New York, 1970.
13. R.I. Jaffee, in Titanium Science and Technology ed. R.I. Jaffee, H.M. Burte, Plenum Press (1973), p.1665.
14. D. Stewart, B.A. Hatt and J.A. Roberts, *Brit. J. of App. Phys.*, 16, 1081 (1965).
15. T.S. Kuan and S.L. Sass, *Acta Met.*, 24, 1053 (1976).
16. H.M. Otte, in 'The Science Technology and Applications of Titanium', Pergamon, New York, 1970, p.645.
- 17(a) S. Banerjee and R. Krishnan, *Acta Met.*, 19, 1317 (1971).
- 17(b) S. Banerjee and R. Krishnan, *Met. Trans.*, 4, 1811 (1973).
18. R.W. Cahn, *Acta Met.*, 1, 49 (1953).
19. D. Defontaine, N.E. Paton and J.C. Williams, *Acta Met.*, 19, 1153 (1971).
20. S.L. Sass, *J. of Less Comm. Metals*, 28, 157 (1972).
21. C.W. Dawson and S.L. Sass, *Met. Trans.*, 1, 2225 (1970).
22. B.A. Hatt and J.A. Roberts, *Acta Met.*, 8, 575 (1960).
23. Sarath Kumar Menon, Sri Kumar Banerjee and Rangachari Krishnan, *Met. Trans.*, 9A, 1213 (1978).
24. C.G. Wilson and D. Sams, *Acta Cryst.*, 14, 71 (1961).
25. J.C. Williams, D. de Fontaine and N.E. Paton, *Met. Trans.*, 4, 2701 (1973).
26. P.G. Shewmon, in 'Transformations in Metals', McGraw Hill, 1969, p.180.
27. H. Jones, Proc. 2nd Int. Conf. on Rapidly Quenched Metals, Cambridge, Massachusetts, 1975, ed. N.J. Grant, B.C. Giessen, vol 1, page 1.
28. D.R. Harbur, J.W. Anderson and W.J. Maraman, *TMS-AIME*, 245 (1969) 1055.
29. W.A. Tiller, K.A. Jackson, J.W. Rutter and B. Chalmers, *Acta Met.*, 1, 428 (1953).
30. H.E. Kissinger, *Annal. Chem.*, 29, 1702 (1957).
31. L.E. Tanner and R. Ray, *Scripta Met.*, 11, 783 (1977).
32. J.W. Chan, *J. Chem. Phys.*, 42, 93 (1965).
33. F.N. Rhines and R.W. Gould, *Adv. in X-ray Analysis*, 6, 62 (1963).
34. W.E. Sweeney Jr. and A.P. Batt, *J. Nucl. Mat.*, 13, 87 (1964).

FIGURE CAPTIONS

- Fig. 1. Cellular α structure (a) BF, (b) DF with α -reflection and (c) DF with silicide reflection.
- Fig. 2. Free energy change (F) versus temperature (T) plot for $\alpha \rightarrow$ liquid and $\beta \rightarrow$ liquid transformations.
- Fig. 3. particles in the matrix of equiaxed grains in Zr-5.5Nb (a) BF (b) SAD (c) Key.
- Fig. 4. $M_S(\alpha)$ and $M_S(\omega)$ temperatures as functions of Nb content.
- Fig. 5. STEM micrograph showing cellular α -structure, qualitative x-ray analysis shows Si enrichment at the cell boundaries.
- Fig. 6. Small-angle boundaries within cells; (a) Unalloyed Zr, (b) Zr-2.5Nb.
- Fig. 7. Martensite laths propagating through cell boundaries in Zr-2.5Nb (a) BF (b) + (c) BF and DF pair showing cell boundary phase within a lath.
- Fig. 8. Fine plates of Zr-5.5Nb martensite in a group of β -cells.
- Fig. 9. SAD patterns showing different variants of α orientations which follow Burger's orientation relation:
- $$(0001)_\alpha // 110_\beta ; \langle 11\bar{2}0 \rangle_\alpha // \langle 111 \rangle_\beta$$
- (a) $[111]_\beta$ zone (b) $[100]_\beta$ zone
- Fig.10. (a) and (b) BF and DF pair showing plate martensite in the background of a cellular structure in Zr-5.5Nb (Si and O-contaminated). Note no plates are crossing cell boundaries.
- Fig.11. Dendritic (a) and cellular (b) structure in Zr-5.5Nb. Martensitic structure is also revealed under polarized light in (b).
- Fig.12. Free energy (G) versus composition (X) plot for the β and the liquid phases in the Zr-Nb system. A and B are tangents to the G^β and G^L curves at the 5.5%Nb concentration. The intercepts of these tangents A and B on X=1 axis (not shown in this schematic drawing) gives the chemical potentials μ_{Nb}^β and μ_{Nb}^L respectively, C is the common tangent to the G^α and the G^β curves.
- Fig.13. Equiaxed grain structure of Zr-20%Nb with no sign of micro-segregation.
- Fig.14. Parallely stacked martensite laths in Zr-2.5%Nb
- Fig.15. (a) BF and (b) DF ($\vec{g} = 0002$) images show dislocation arrays at the small angle boundaries between adjacent laths (c) superimposed diffraction patterns from a pair of $10\bar{1}1$ twin related martensite laths (d) alternate black white contrast of a group of twin related laths.
- Fig.16. Internally twinned plate martensite in Zr-5.5Nb.
- Fig.17. $\{10\bar{1}1\}$ internal twins in a martensite plate in Zr-5.5%Nb

- Fig.18. (a) BF and (b) DF showing internal twins. A second variant of $10\bar{1}1$ twin is seen in the area marked X.
- Fig.19. BF (a) and DF (b) images show a set of internal twins propagating from one martensite plate to another (c) shows ω pattern (110_{β} zone, key given in Fig.3), obtained from a region adjacent to the plates shown in (a) and (b).
- Fig.20. Morphology of ω -particles in Zr-5.5Nb.
- Fig.21. Isolated martensite plates in β grains containing ω particles in Zr-5.5Nb.
- Fig.22. SAD pattern in (b) can be indexed in terms of superimposed reciprocal lattice sections of β and α , the Burger's orientation relation being obeyed. DF with α reflections reveal the morphology of these α particles (a) Refer. Fig. 9(b) for key.
- Fig.23. DF image showing ω particles in β matrix in Zr-10Nb. SAD shows superimposition of four ω -variants.
- Fig.24. Extra reflections at $\frac{1}{2}\{110\}_{\beta}$ and $\{100\}$ positions in Zr-10Nb.
- Fig.25. Diffuse intensity along $\{111\}$ reciprocal lattice places (a) close to $[311]_{\beta}$ zone (b) $[110]_{\beta}$ zone.
- Fig.26. (a) β'' plates imaged by polarised light microscopy. (b) β'' plates in BF TEM image, (c) DF image using ω -reflection, shows a denser population of ω particles along β'' plates.
- Fig.27. (a) Morphology of β grains of the splat quenched Zr-27at%Al alloy (b) BF and (c) DF images show uniform distribution of precipitates within these grains.
- Fig.28. DF image with a precipitate reflection reveals a cellular structure within a few grains of the splat-quenched Zr-27%Al alloy.
- Fig.29. Appearance of extra spots at $\frac{1}{3}$ bcc positions in the SAD patterns taken from Zr-27%Al: (a) $[210]$ zone, (b) $[311]$ zone.
- Fig.30. (a) $[111]_{\beta}$ zone. Faint spots close to the central spots are $\{10\bar{1}0\}$ reflections which are associated with zero structure factor and can not appear due to double diffraction in this zone. (b) $[001]_{\beta}$ zone. Forbidden $[010]_{\beta}$ spots can not be accounted as ω -reflections.
- Fig.31. (111) stacking sequence in bcc, ω and Zr_2Al . Note that by collapsing atomic layers numbered 1 and 2, 4 and 5, it is possible to generate the right sequence for the ω and the Zr_2Al structures.
- Fig.32. (a) Alignment of ordered particles along $\{100\}$ planes (b) corresponding SAD $[001]_{\beta}$ zone, key shown in Fig. 30(b) in which the intensity distribution at each spot is schematically shown (c) the right hand side grain shows modulations along 100 planes in DF with a fundamental reflection ($g = 100$) while the left hand side grain which is not oriented along $\langle 100 \rangle$ zone shows random distribution of ordered particles in a superlattice DF.
- Fig.33. Atomistic representation of the $\beta \rightarrow \omega$ transformation (a) bcc structure projected on (111) plane, (c) atoms in the plane

of the figure (+) above and (-) below the plane, (b) (111) planes on edge showing bcc stacking sequence ABCABC, (c) (111) plane projection after double plane collapse to give, ω -structure with the stacking sequence AB'AB', filled circle representing B' plane, (d) displacement wave description. (Ref. 25).

- Fig. 34. Mechanism of formation of Zr_2Al in β lattice. Description A involves collapse of (111) planes followed by replacement of atoms to produce the ordered structure. Description B involved setting up of a concentration wave in the β lattice followed by collapse of (111) planes. The development of concentration wave is shown by three traces corresponding to times t_0 , t_1 and t_2 where $t_2 > t_1 > t_0$.
- Fig. 35. Dendrites in amorphous matrix in Zr-24%Ni.
- Fig. 36. Martensitic (a) and omega (b) structures within the dendrites.
- Fig. 37. Hypothetical G-X plot shows the composition range ($X_1 < X < X_2$) of the β phase which can nucleate from a moderately undercooled liquid.
- Fig. 38. (a) X-ray diffraction data (intensity versus 2θ plot) on as melt spun (1) and crystallized (2 and 3) Zr-24a/oNi samples. Traces 2 and 3 correspond to samples which have gone through the event I and II respectively, (b) electron diffraction pattern from the amorphous matrix of Zr-24a/oNi, (c) Micrograph showing a crystalline particle in the amorphous matrix.
- Fig. 39. DSC trace (H, rate of heat evolution, versus temperature) showing two distinct events occurring during continuous heating. T_g is the glass-transition temperature.
- Fig. 40. Microstructures and diffraction patterns of Zr-24a/oNi after different stages of crystallization (a) BF, (b) DF using a segment of the cluster of intense rings and (c) diffraction pattern after the event I, (d) and (e) are BF and diffraction patterns after the event II.
- Fig. 41. Lamellar structure in the gap between α grains.
- Fig. 42. Kissinger plot for determination of activation energies associated with the events I and II in Zr-24a/oNi and the only crystallization event in Zr-24a/oFe.
- Fig. 43. Heterogeneous nucleation of α crystals on the pre-existing crystalline particles.
- Fig. 44. (a) X-ray diffraction results on melt spun Zr-24a/oFe alloy (1). Traces (2) and (3) correspond to the samples which have crystallized to different extents (approximately 30% and 100% respectively). (b) Electron diffraction pattern from the amorphous Zr-24%Fe alloy.
- Fig. 45. Modulated structure of the amorphous Zr-24a/oFe alloy.
- Fig. 46. DSC trace (H versus temperature) showing a single stage crystallization in Zr-24a/oFe.
- Fig. 47. Microstructure, BF(a), and DF(b), and SAD pattern, (c), of Zr-24a/oFe after about 30% crystallization.

Fig. 48. Composite crystals with a geometrical morphology 'Sunflowers'; (a) and (b) BF, (c) DF corresponding to (b), shows two pairs of twin-related petals in contrast. (d) Kikuchi star corresponding to $[111]\beta$ zone; SAD corresponding to (b).

Fig. 49. (a) 'Sunflower' crystal with the central β -core. (b) ω particles within the β core revealed in DF using diffuse ω -reflection.

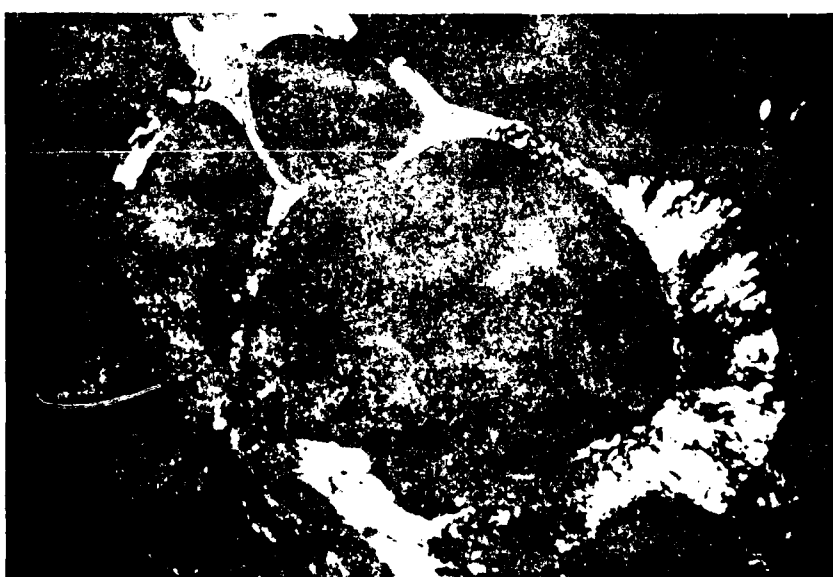
Fig. 50. Crystallographic description of the 'Sunflower' crystal shown in Fig. 49.



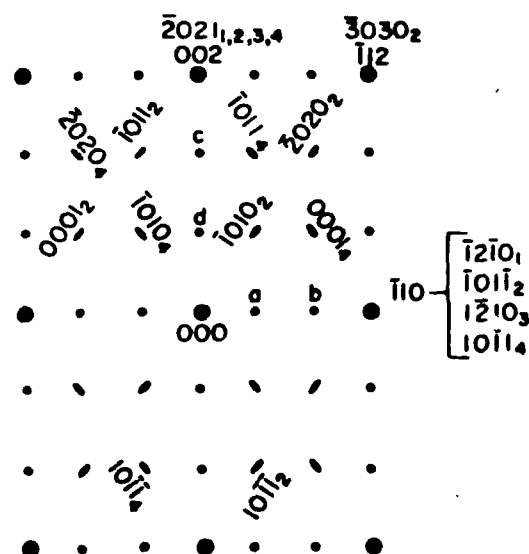
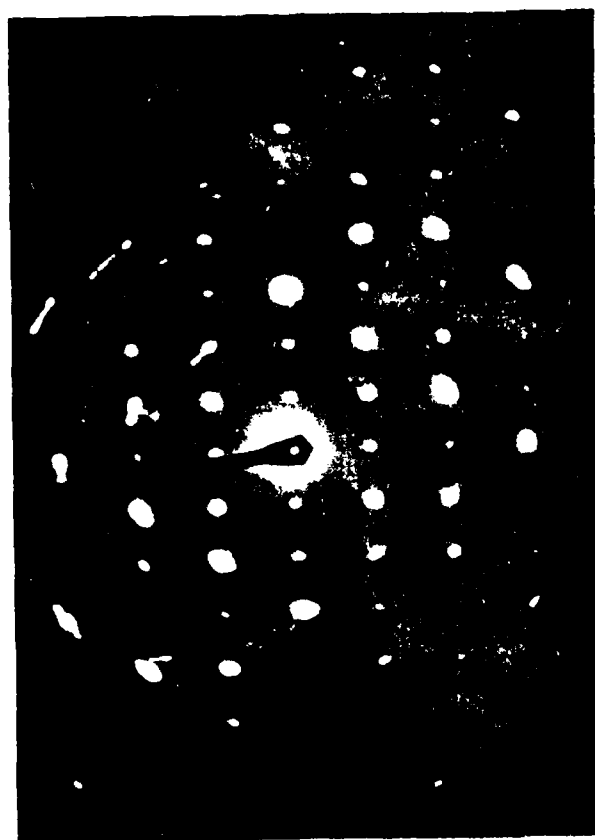
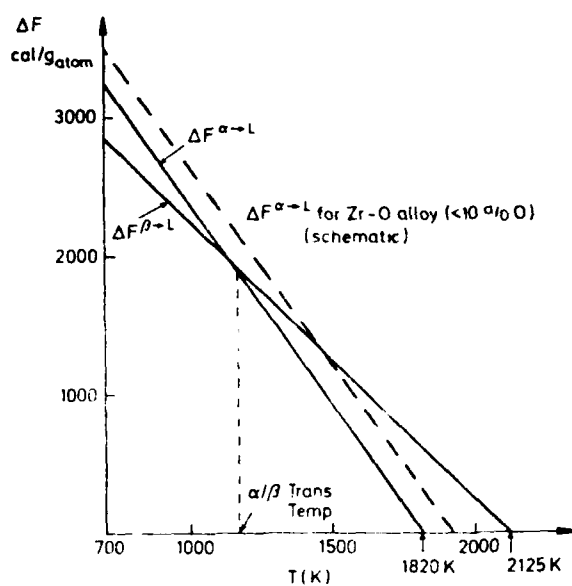
(a)



(b)



(c)



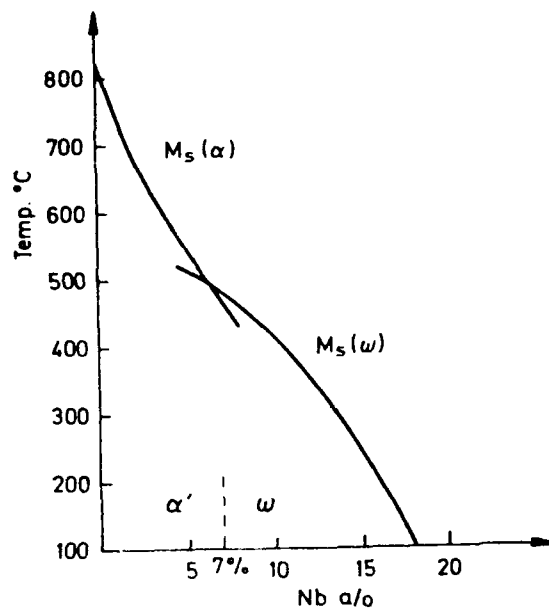


Fig.4

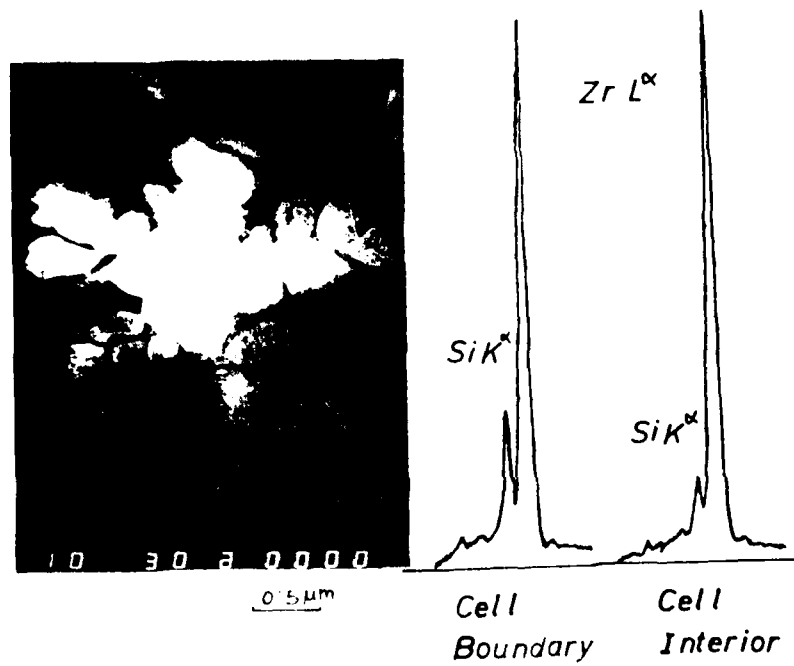
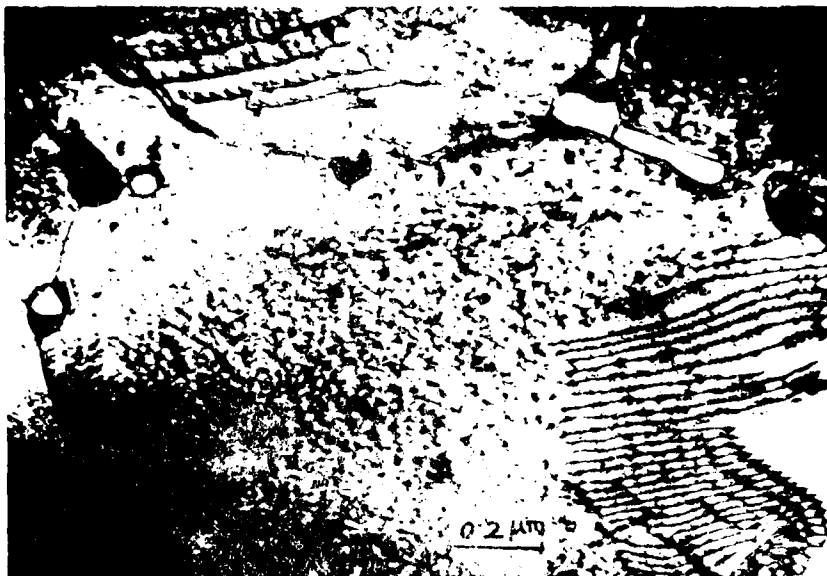


Fig.5

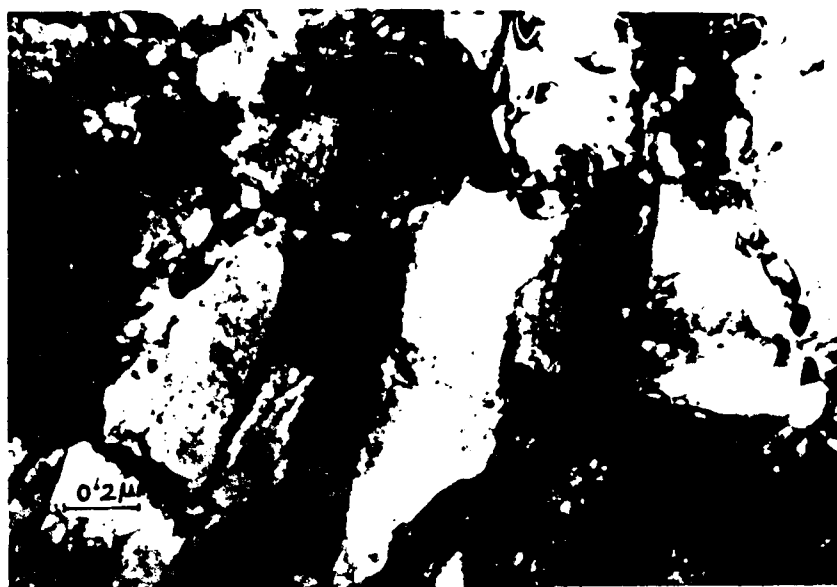


(a7)



(a)

FIG. 6



(a)



(b)

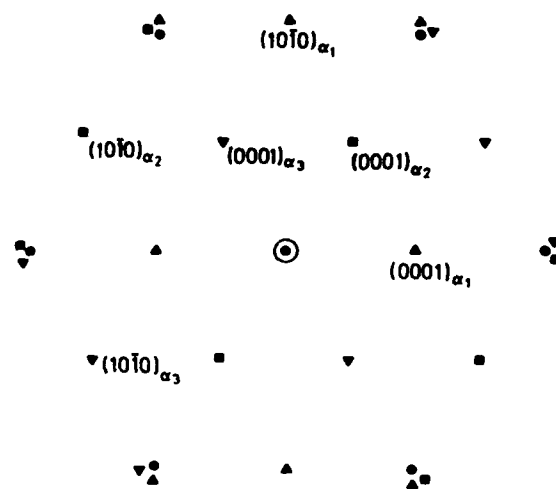


(c)

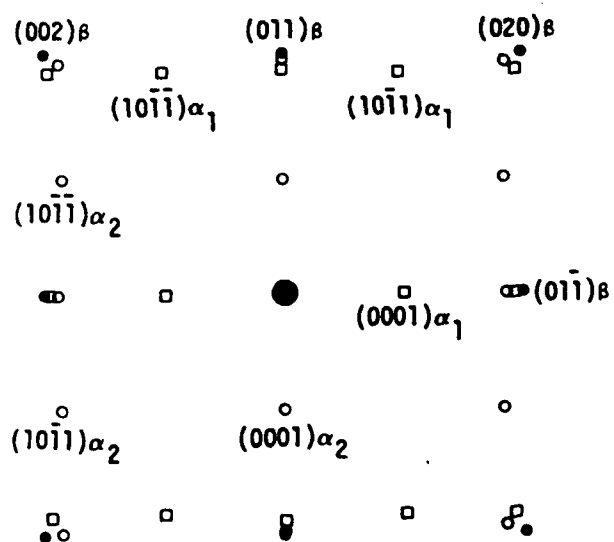
Fig.7



Fig.8



(a)



(b)

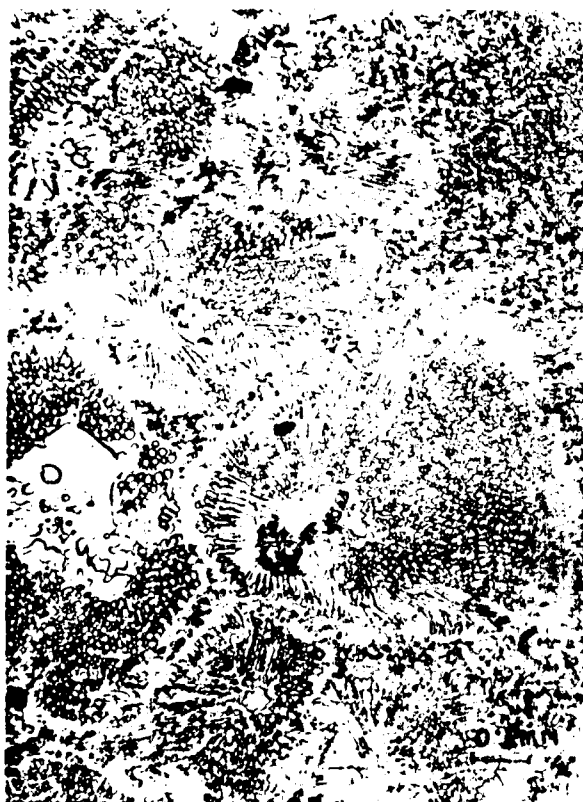


(a)



(b)

Fig. 10



(a)



(b)

Fig. 11

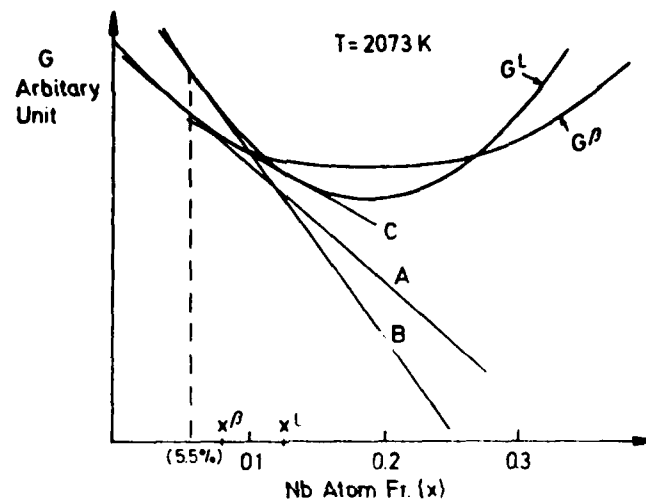


Fig12



Fig.13

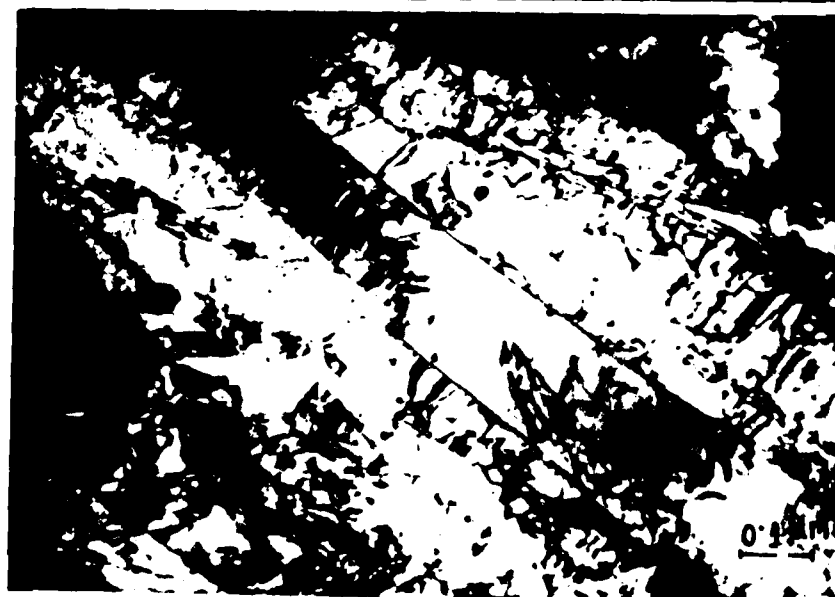


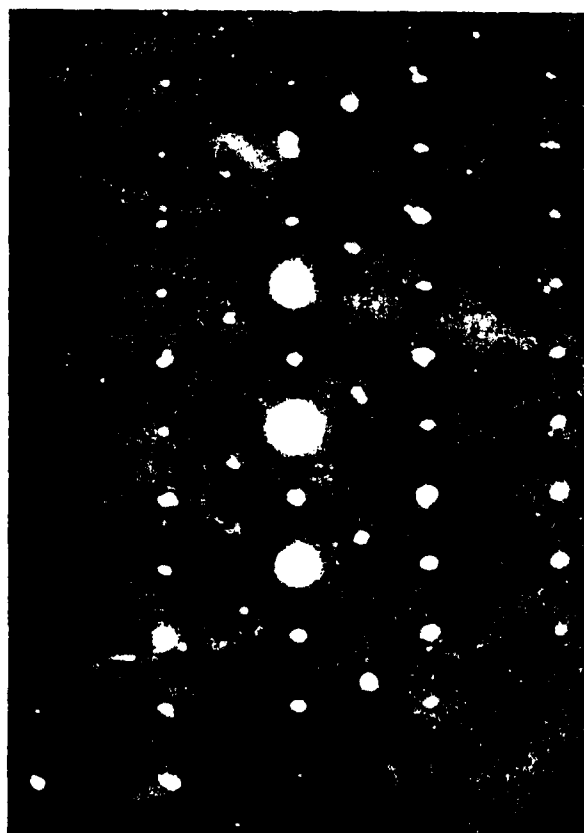
Fig. 14



(a)



(b)



(c)

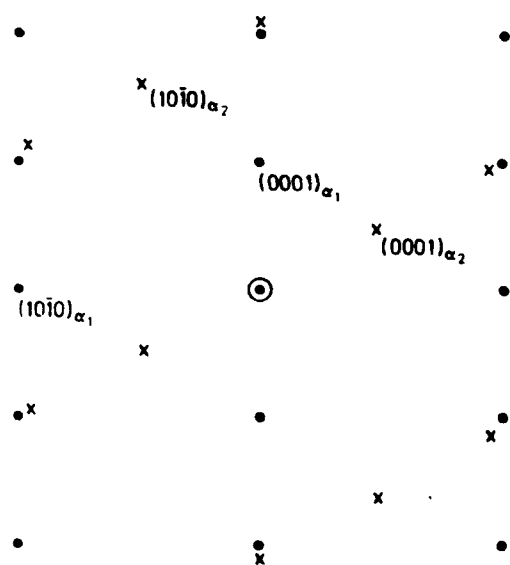


Fig.15



Fig.15(d)



Fig.16

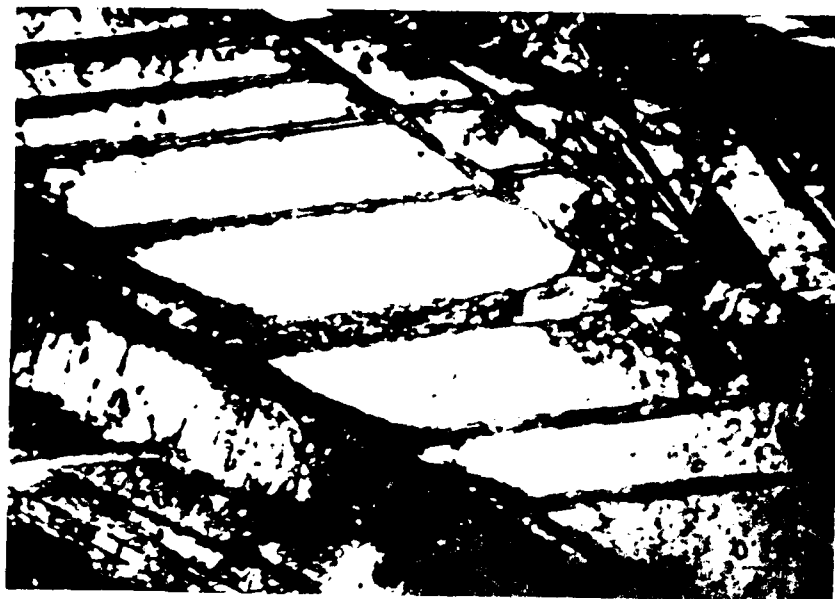


Fig. 17



(a)



(b)

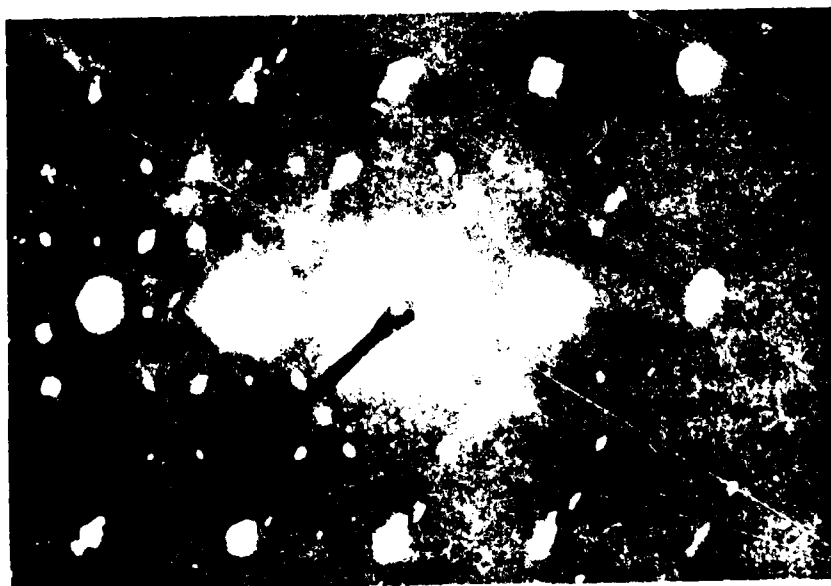
Fig. 18



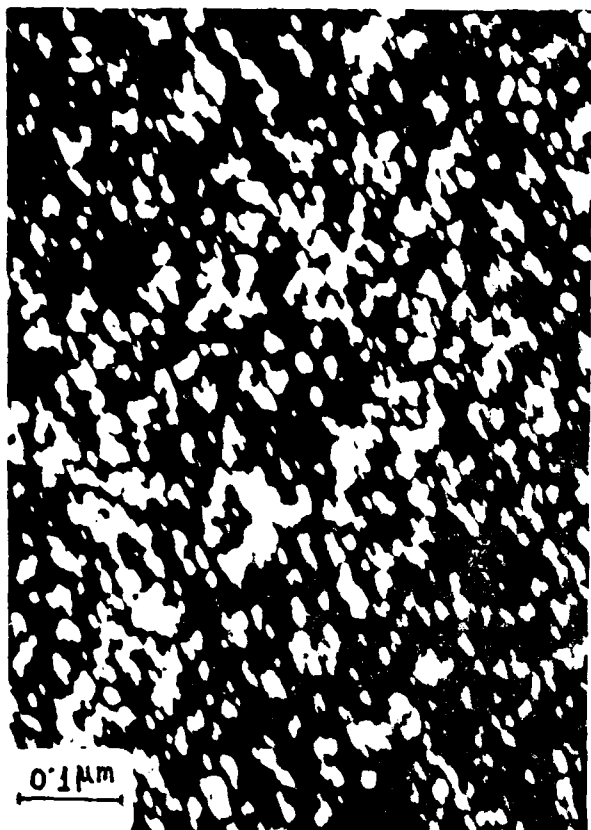
(a)



(b)



(c)



(a)

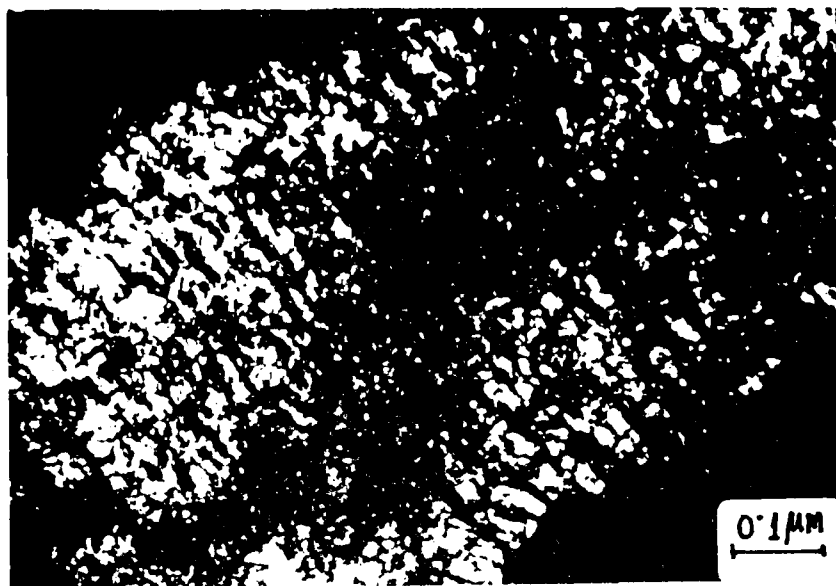


(b)

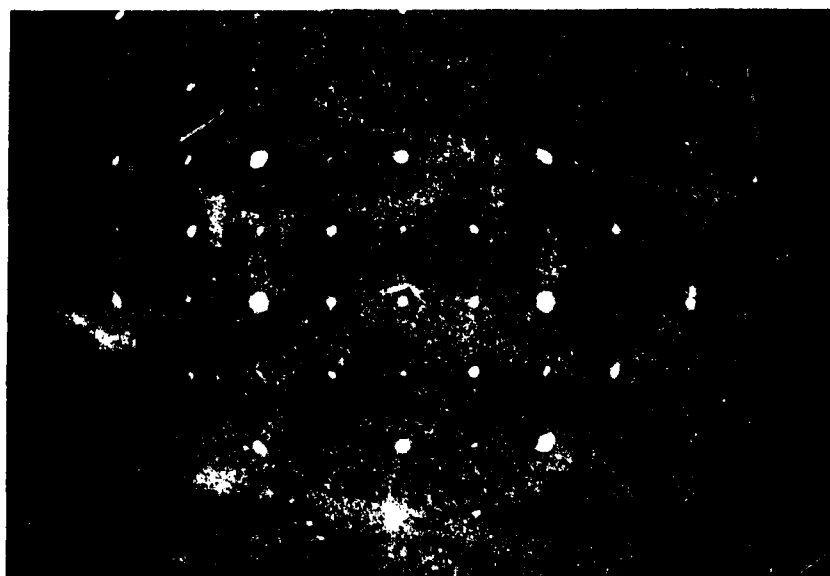
Fig. 20



Fig. 21

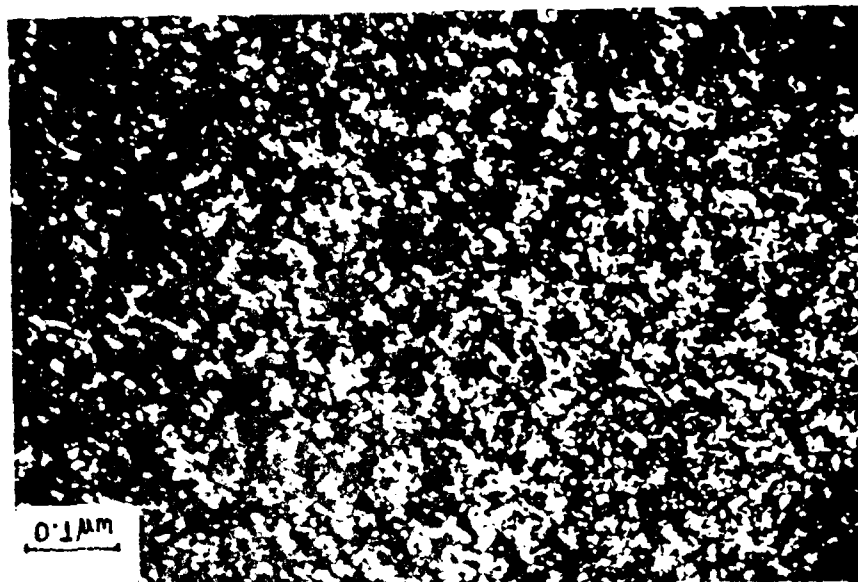


(a)



(b)

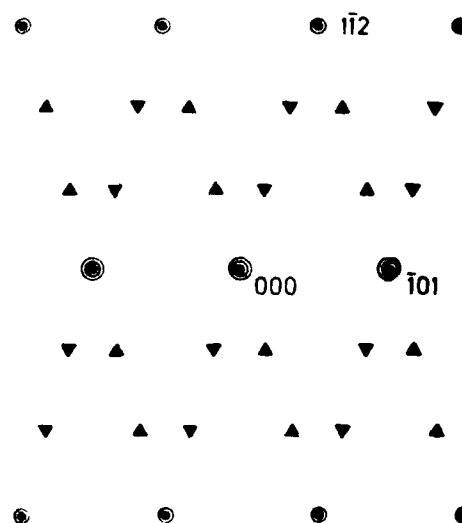
Fig. 22



(a)



(b)



- $[131]_{\beta}$ Z.N.
- $\omega_1 - [10\bar{1}5]_{\omega}$ Z.N.
- ▲ $\omega_2 - [\bar{1}2\bar{1}3]_{\omega}$ Z.N.
- ▼ $\omega_3 - [1\bar{2}13]_{\omega}$ Z.N.
- ω_4 - one line of reflections

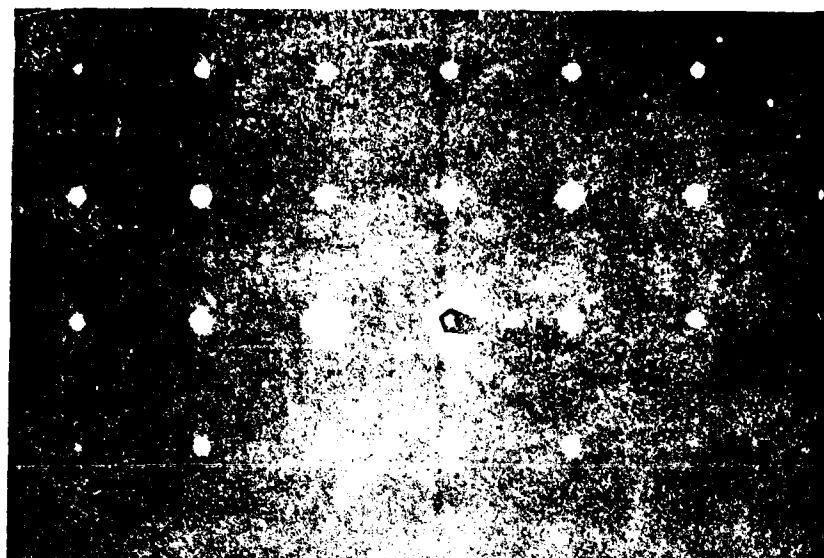
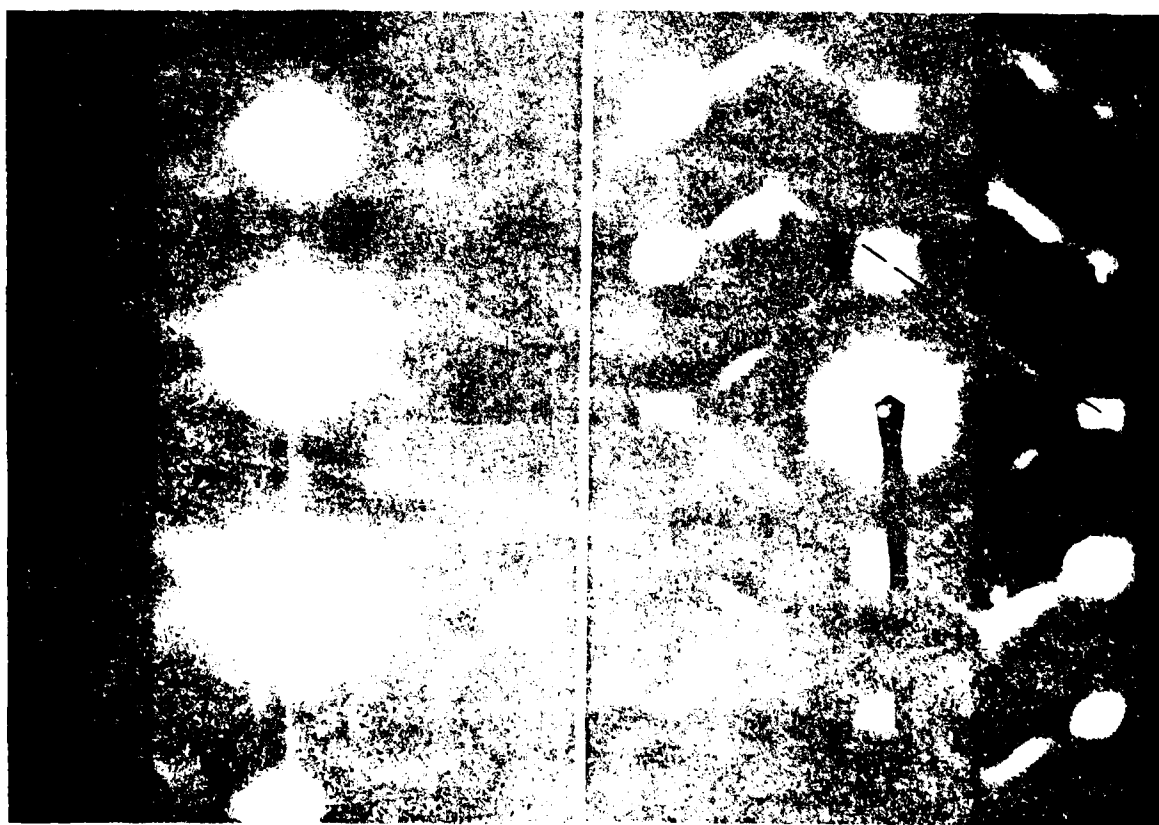


Fig. 2



(a)

(b)



(a)



(c)



(d)

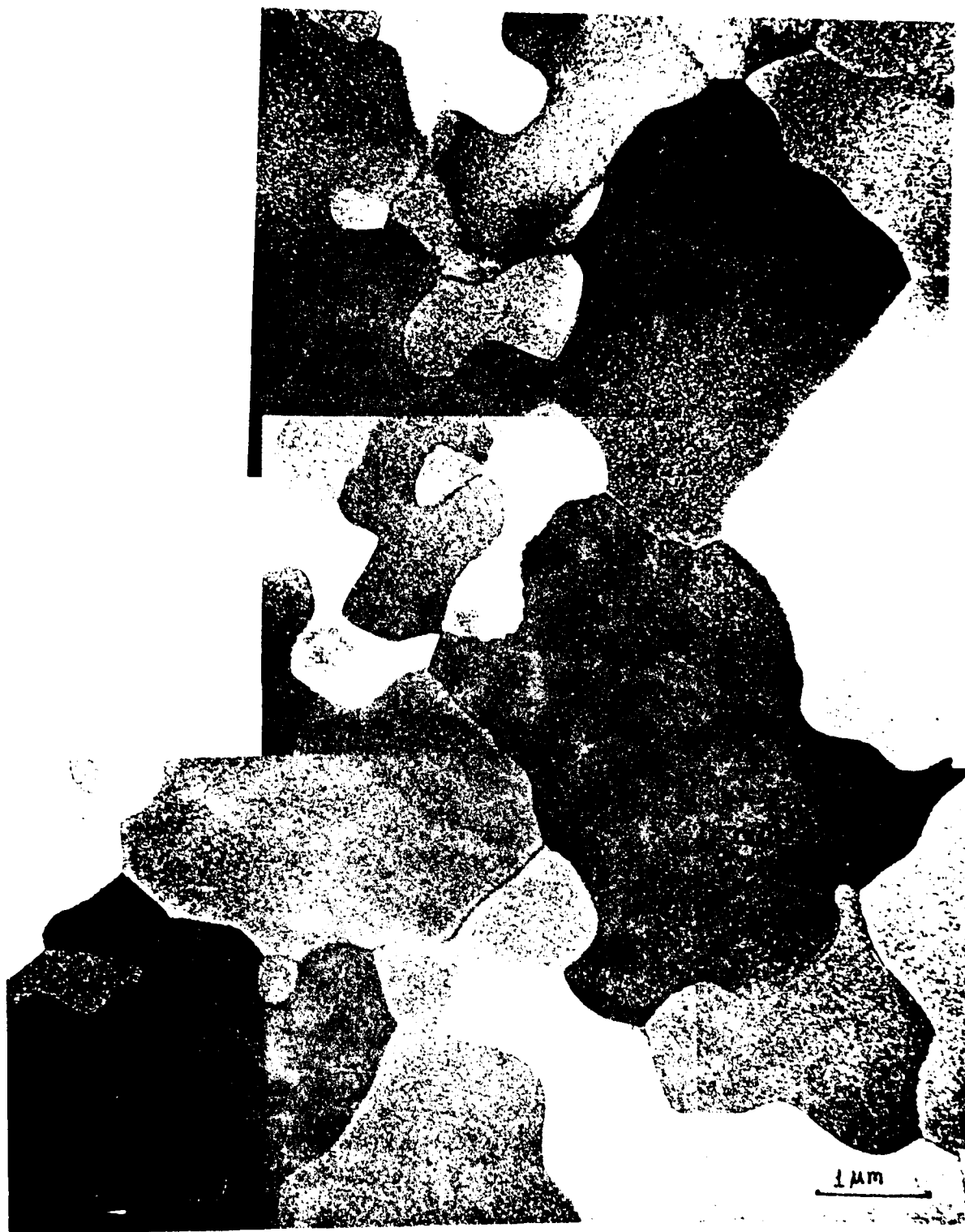


Fig. 27(a)



(b)



(c)

Fig. 27

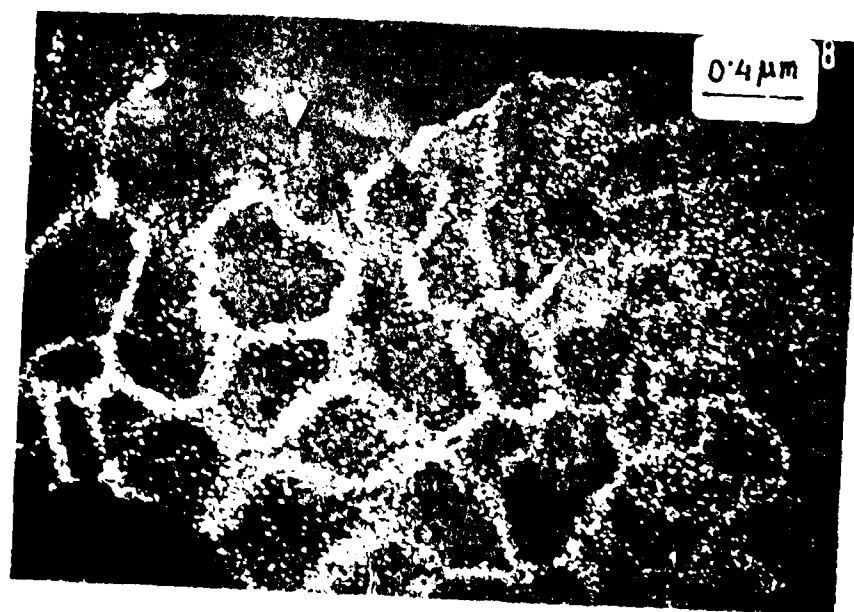
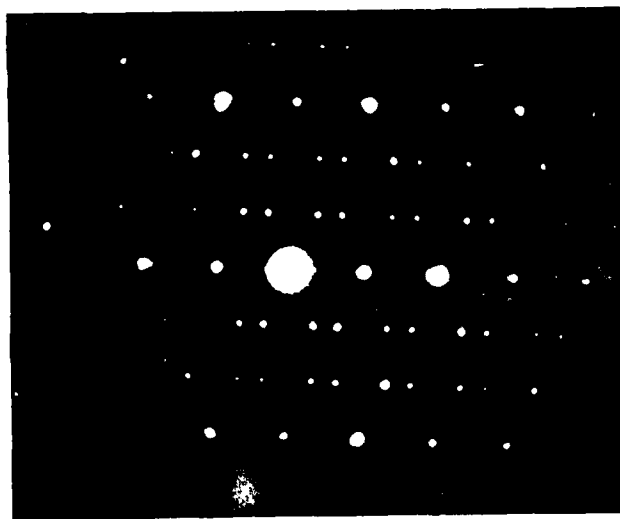
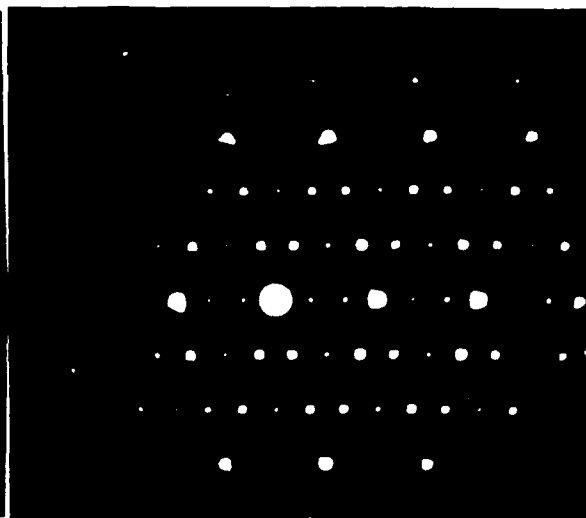


Fig. 28

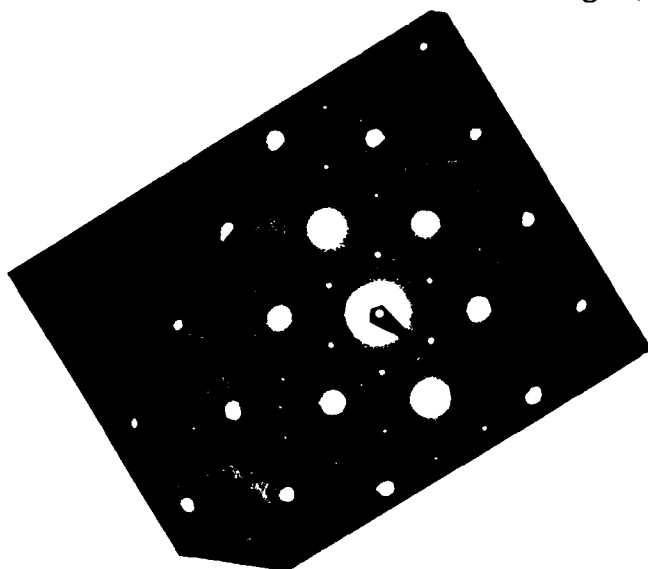


(a)

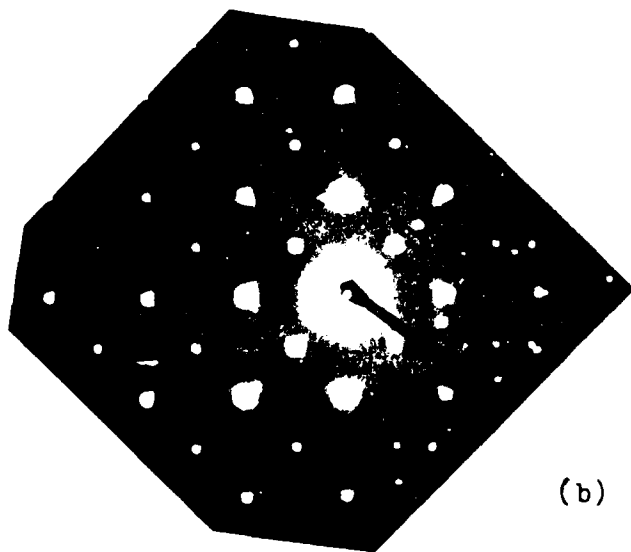
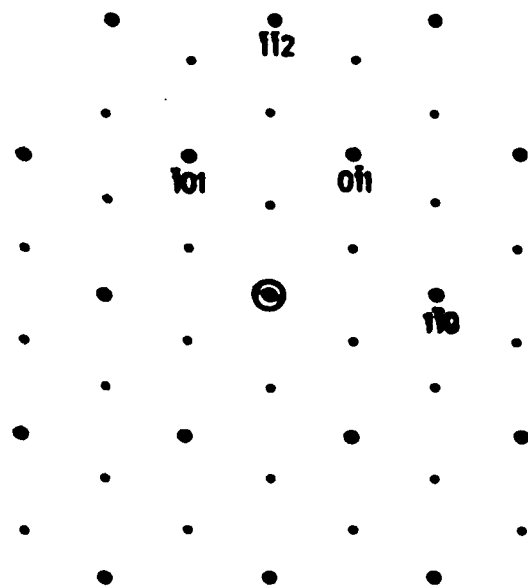


(b)

Fig.29



(a)



(b)

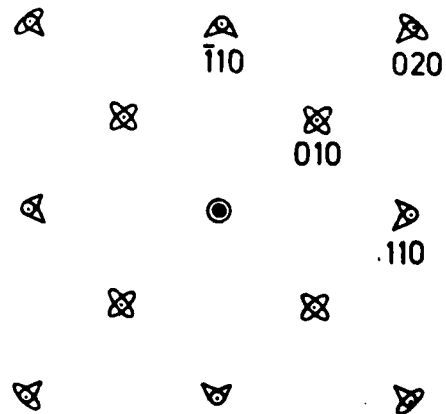


Fig.30

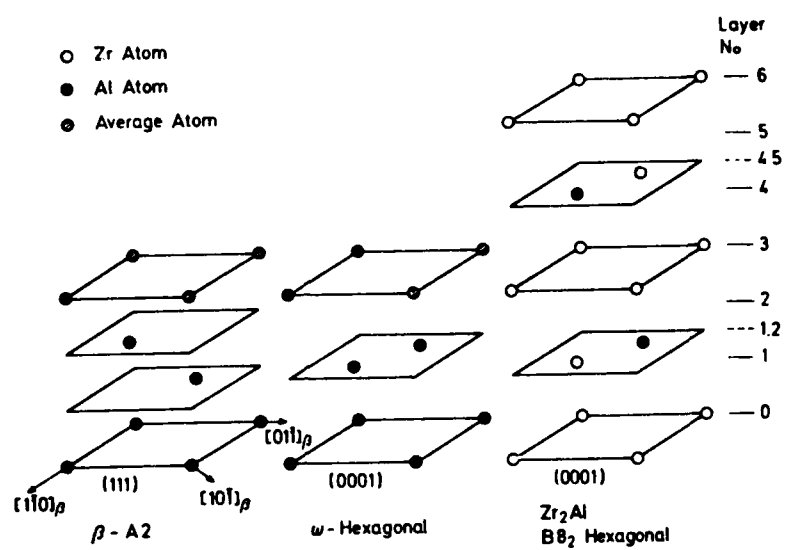
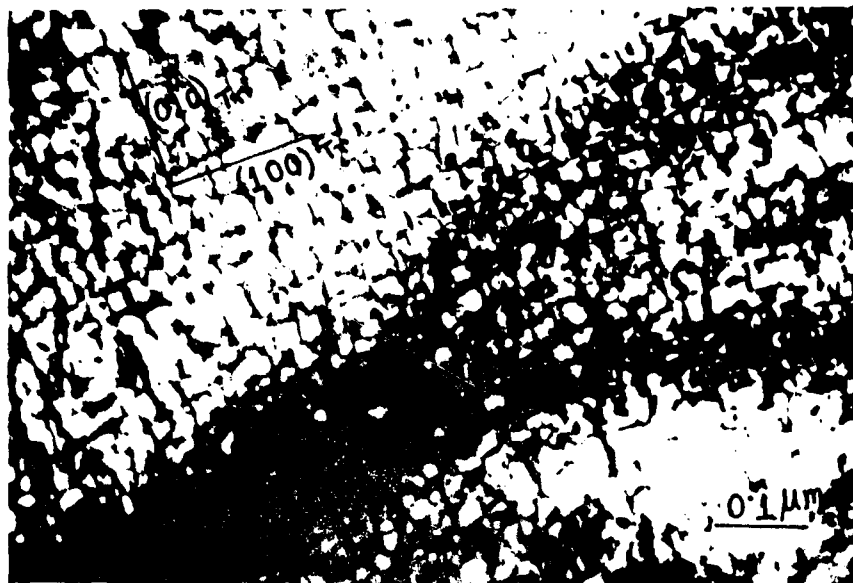
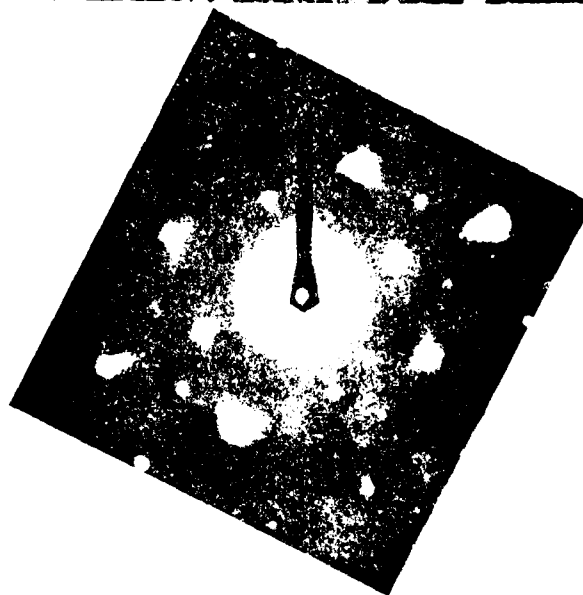


Fig.31



(a)



(b)



(c)

Fig.32

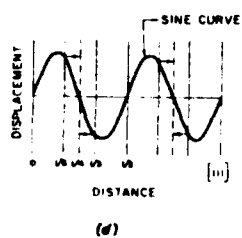
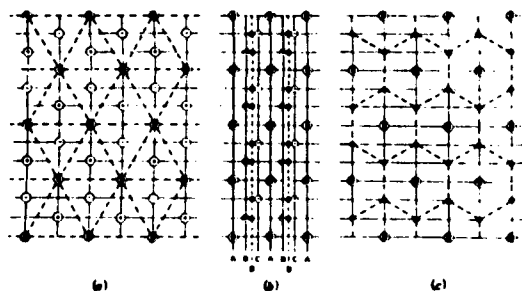


Fig.33

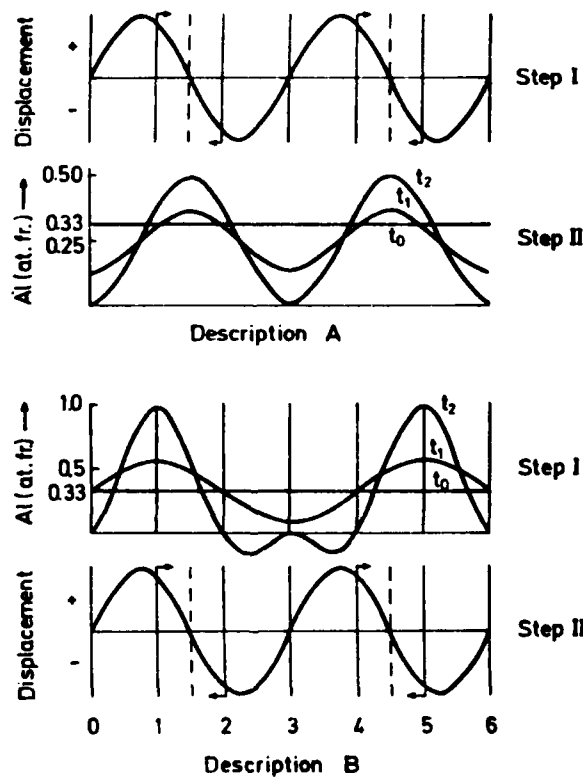
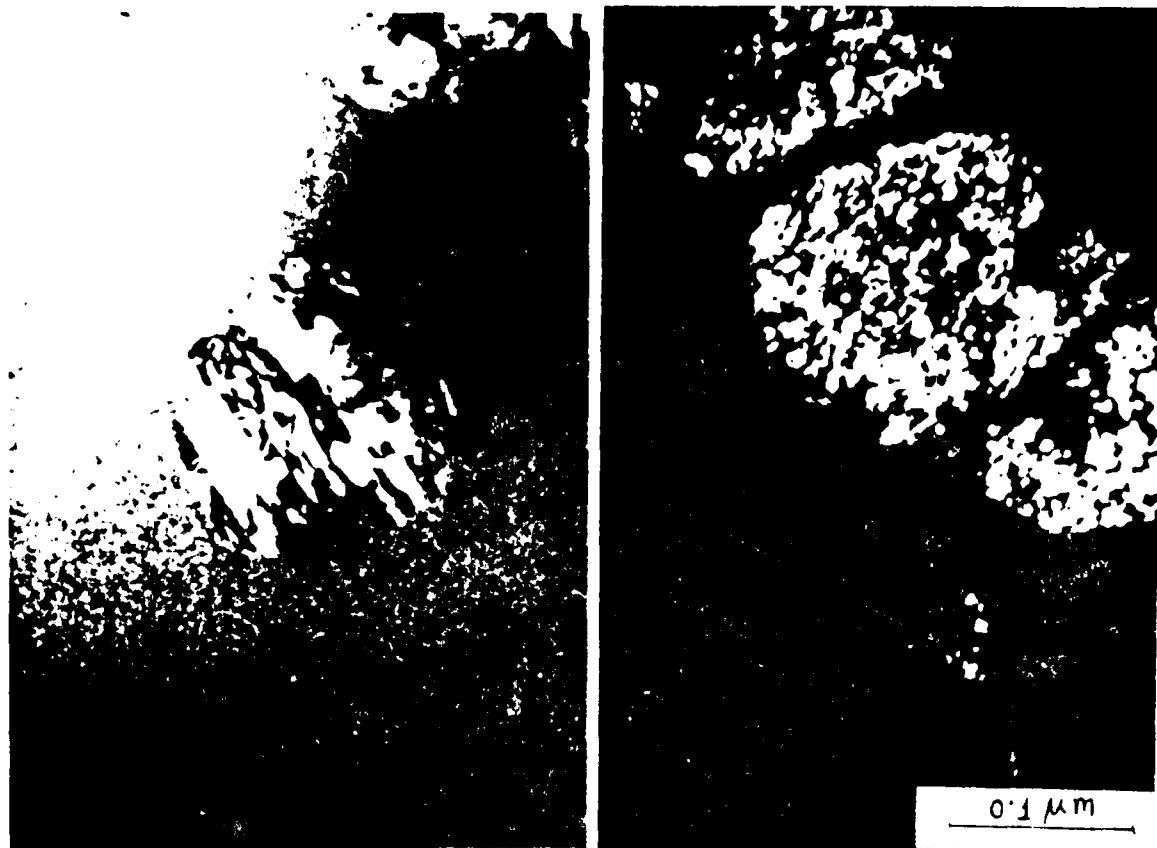


Fig.34



Fig.35



(a)

(b)

Fig.36

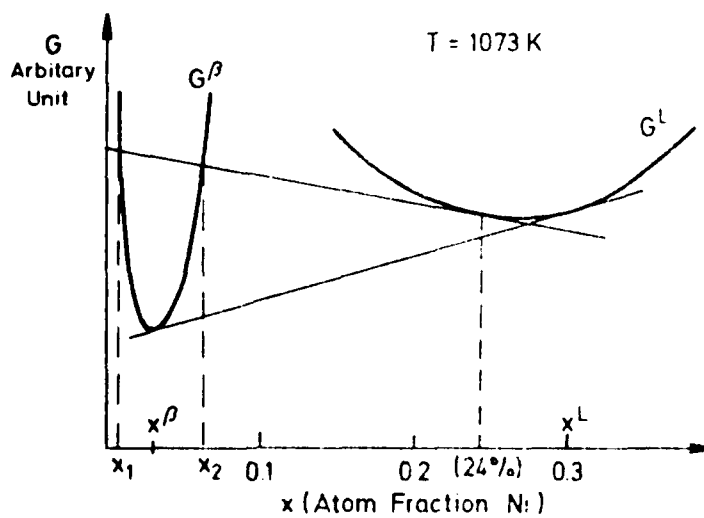
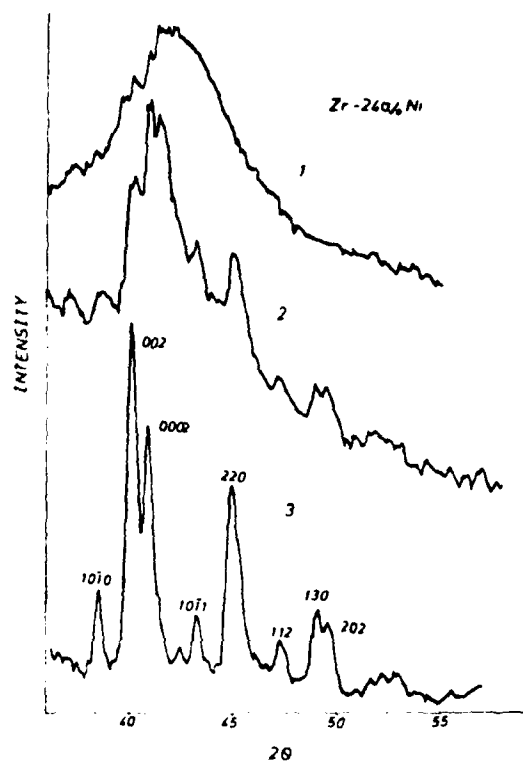
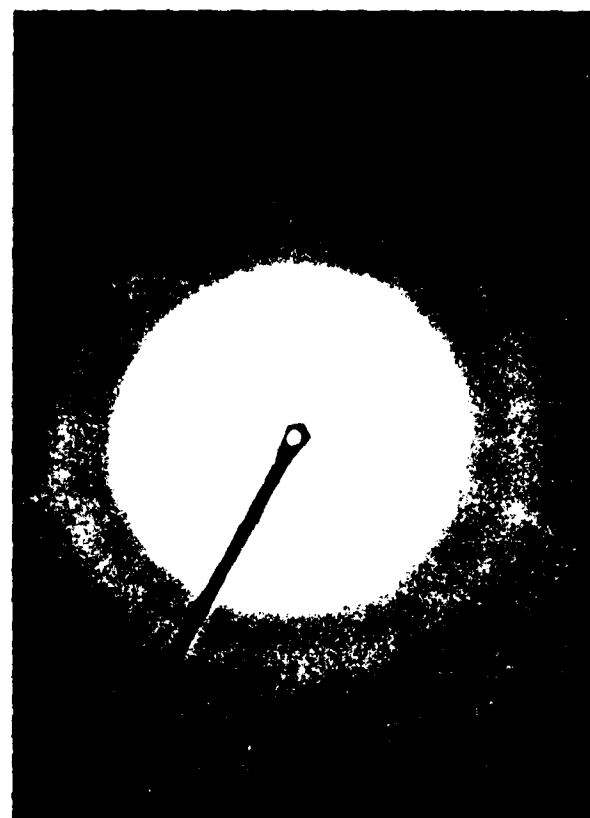


Fig.37



(a)



(b)



(c)

Fig. 38

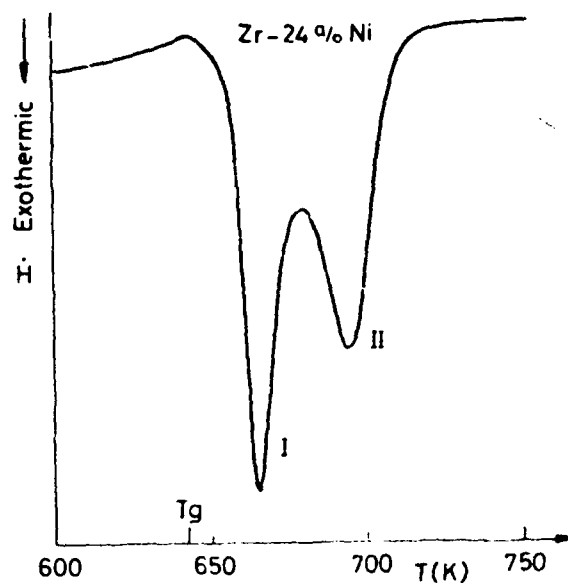
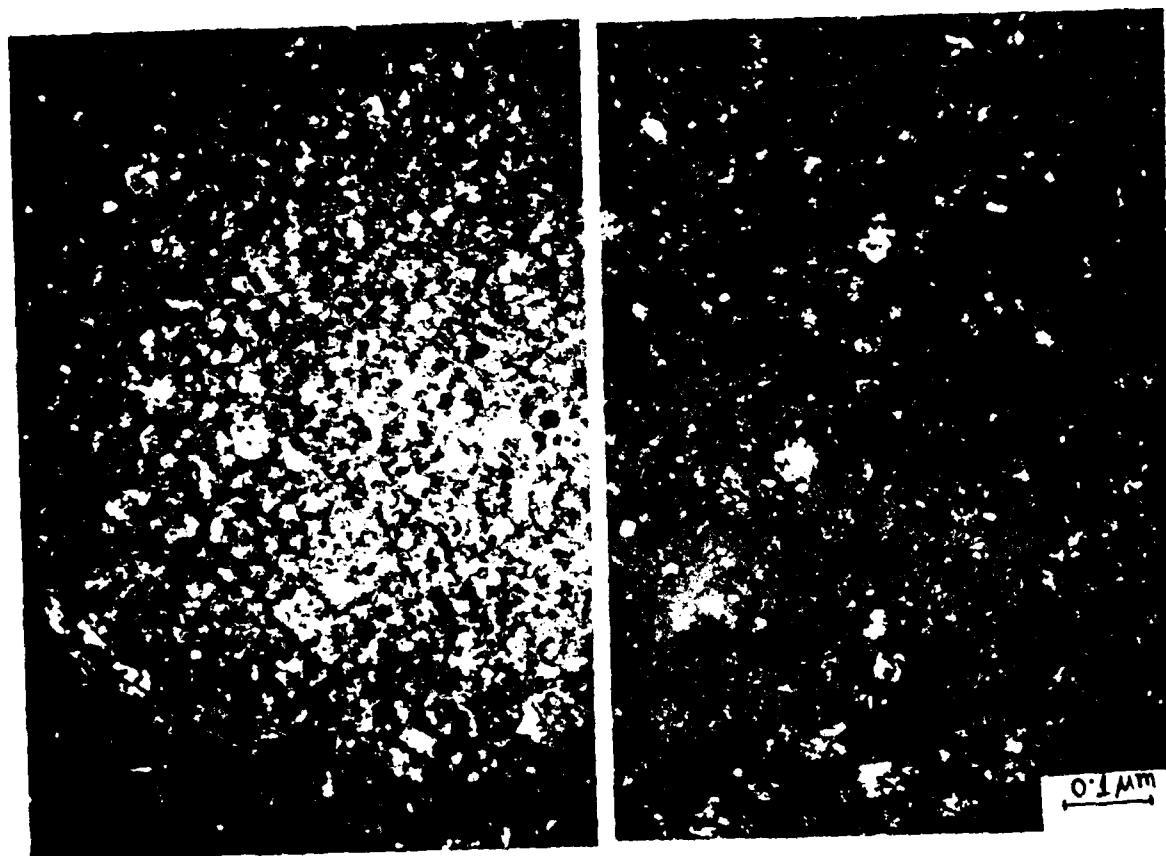


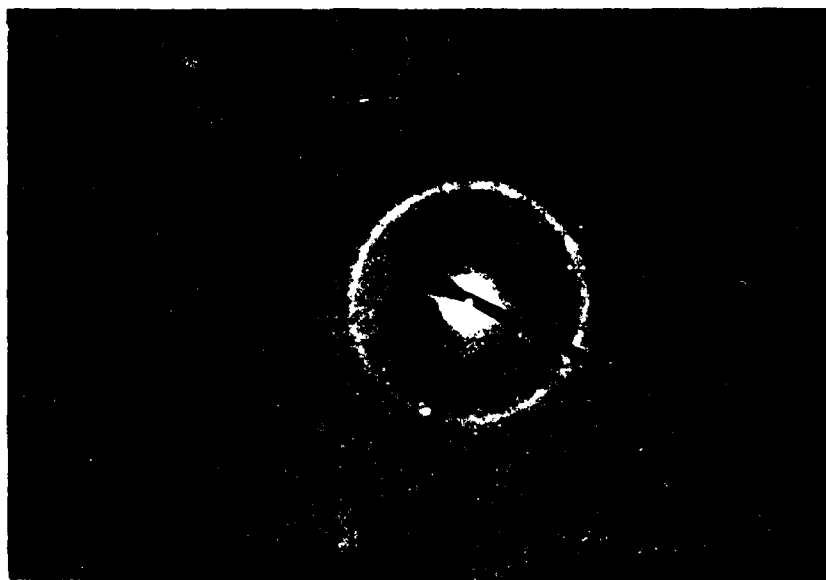
Fig.39



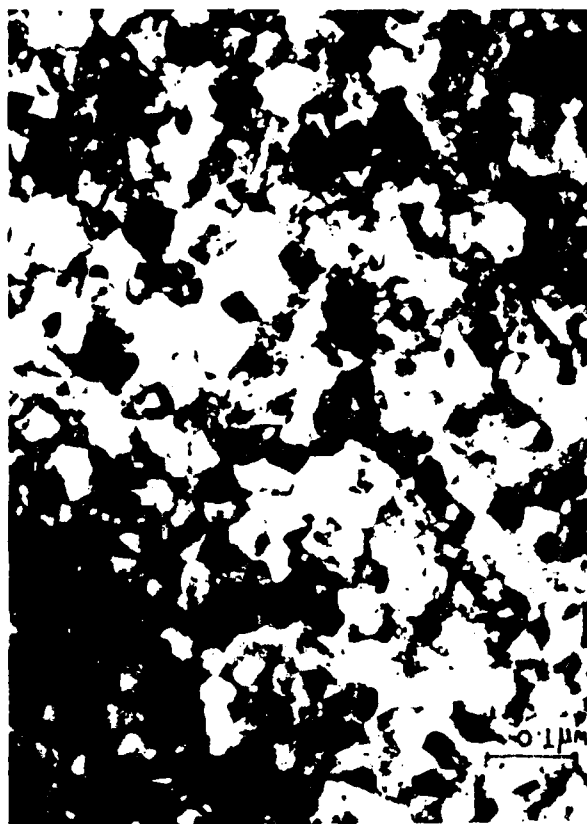
(a)

(b)

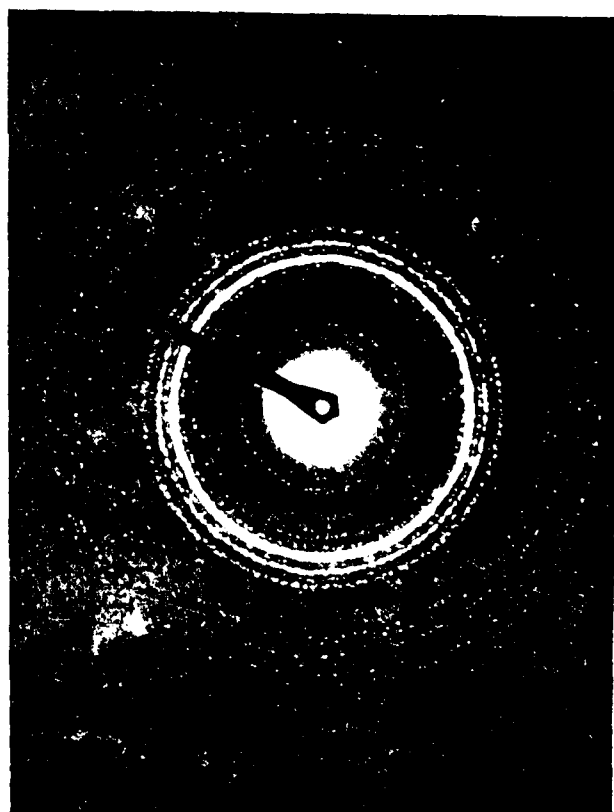
Fig.40



(c)



(d)



(e)

Fig.40



Fig.41

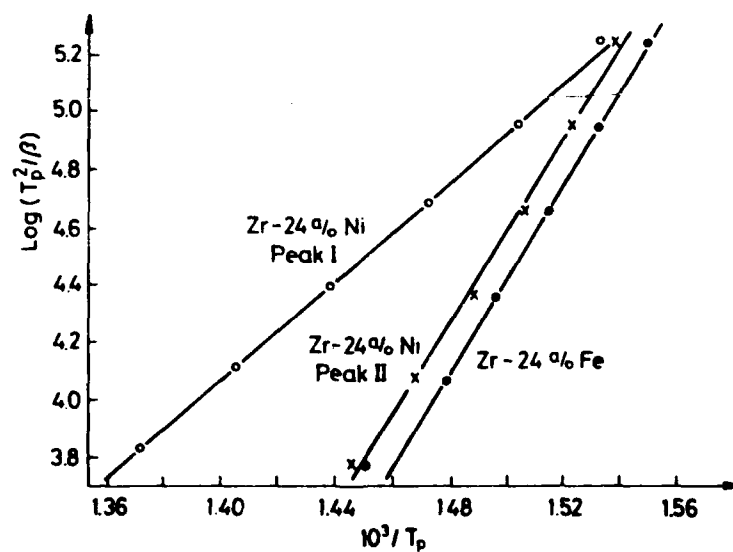
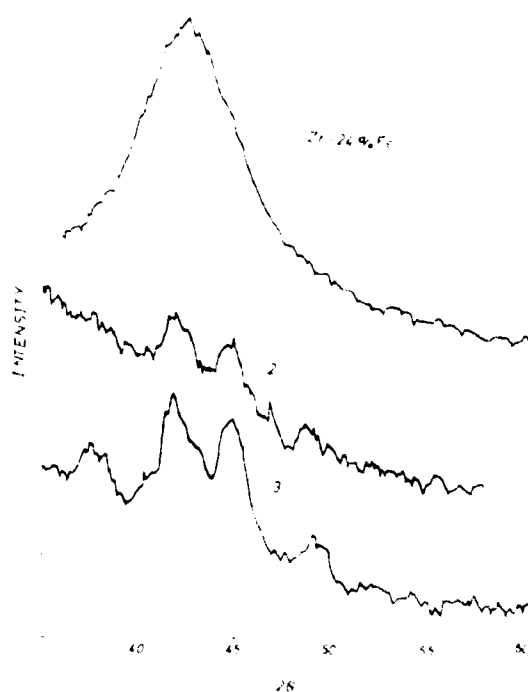


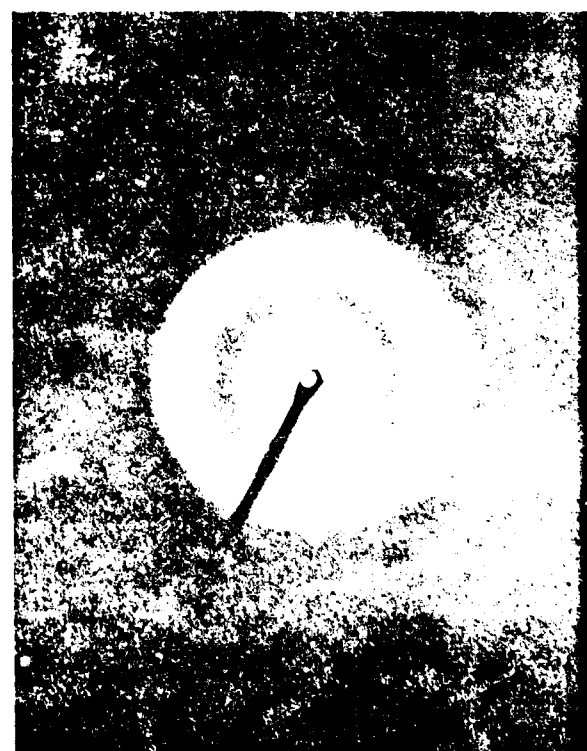
Fig.42



Fig. 43



(a)



(b)

Fig. 44

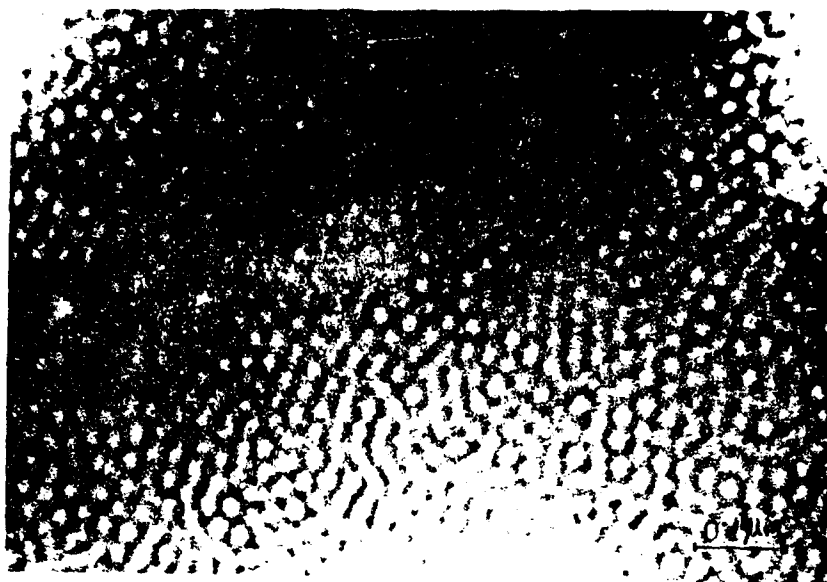


Fig. 45

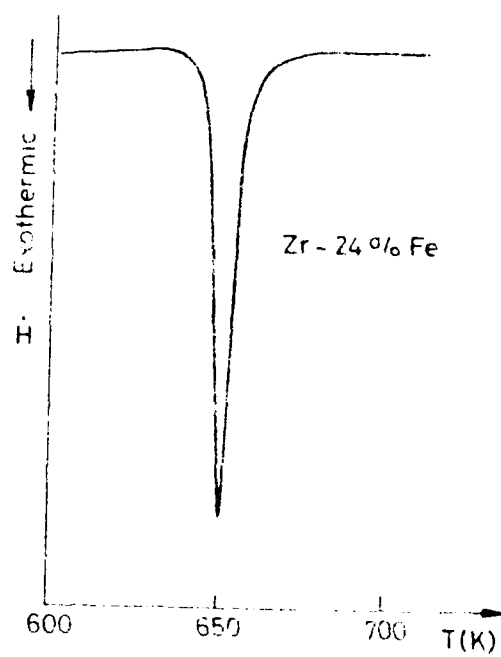
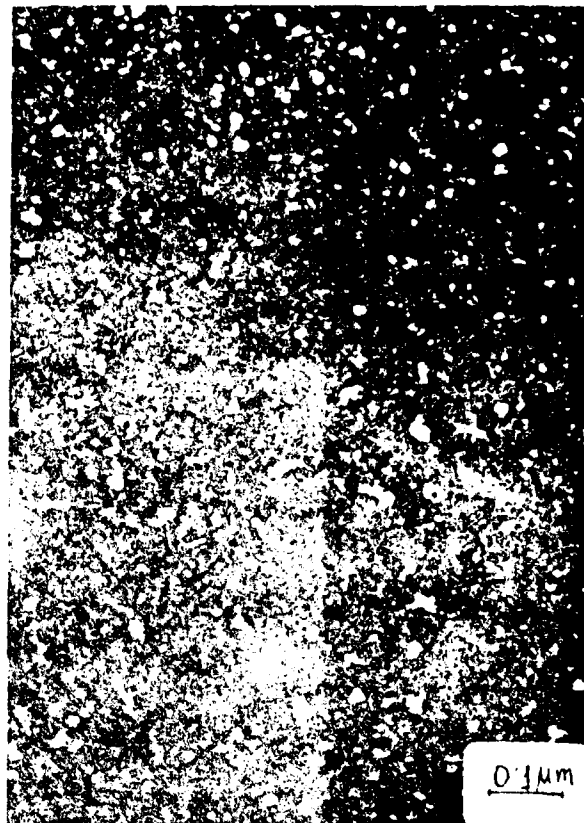
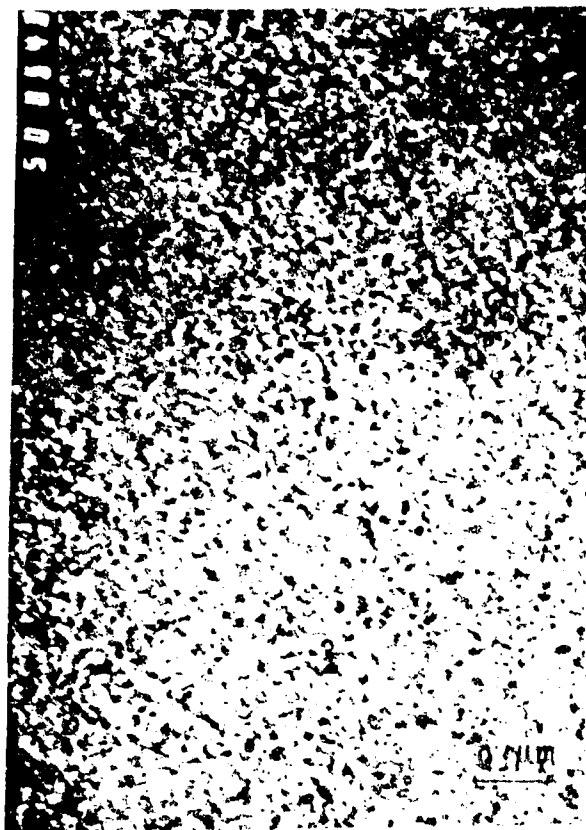
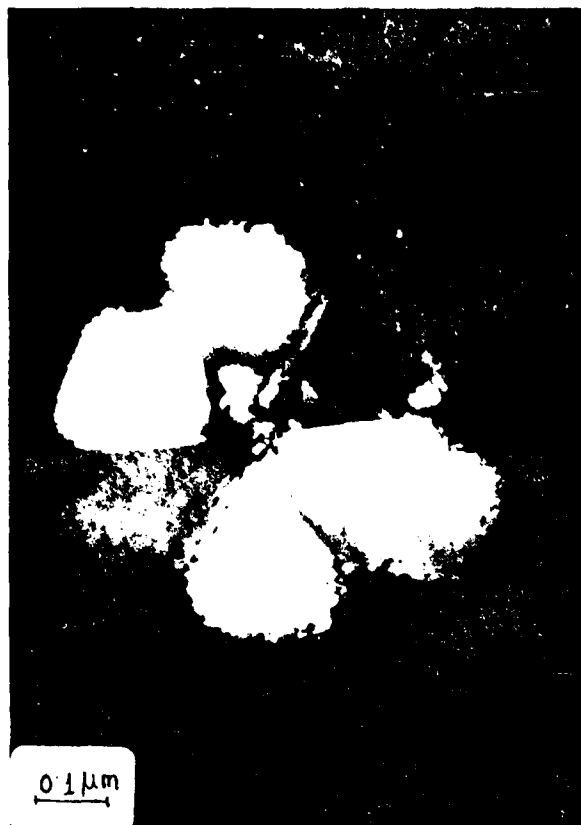


Fig. 46





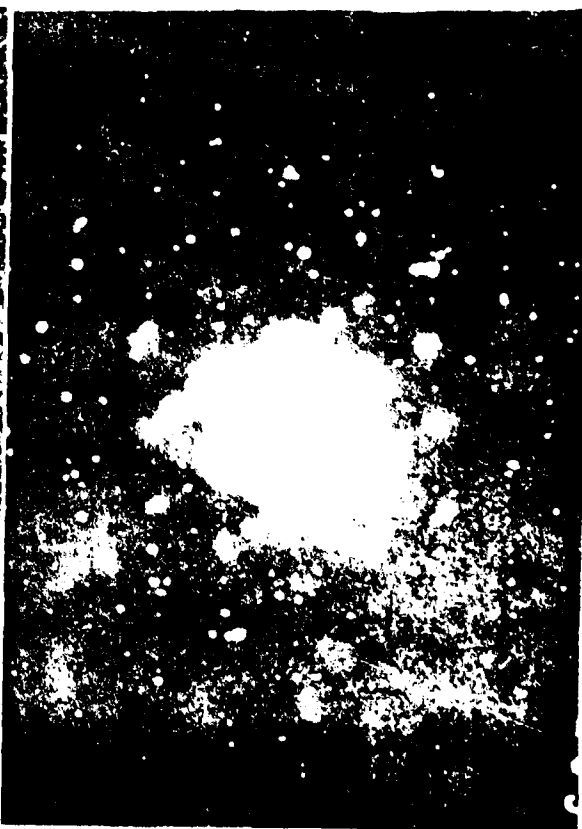
(a)



(b)



(c)



(d)

Fig.48



(a)



(b)

Fig. 49

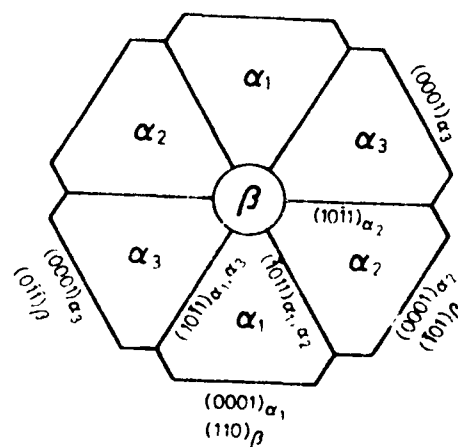


Fig. 50

[illegible]

A

DATE
FILMED
8-8